

Tissue Optics and Photonics: Light-Tissue Interaction II

Valery V. Tuchin^{1,2,3}

¹ Saratov National Research State University, 83 Astrakhanskaya str., Saratov 410012, Russia

² Institute of Precision Mechanics and Control RAS, 24 Rabochaya str., Saratov 410028, Russia

³ Samara National Research University, 34 Moskovskoye Shosse, Samara 443086, Russia

e-mail: tuchinvv@mail.ru

Abstract. This is the third part of the review-tutorial paper describing fundamentals of tissue optics and photonics. The first part of the paper was mostly devoted to description of tissue structures and their specificity related to interactions with light [1]. The second part presented light-tissue interactions originated from tissue dispersion, scattering, and absorption properties, including light reflection and refraction, absorption, elastic, and quasi-elastic scattering [2]. This last part of the paper, underlines mostly photothermal and nonlinear interactions such as temperature rise and tissue damage, photoacoustic and acoustooptical, nonlinear sonoluminescence, Raman scattering, multiphoton autofluorescence, second harmonic generation (SHG), terahertz (THz) radiation interactions, and finally photochemical interactions with description of two widely spread therapeutic applications: photodynamic therapy (PDT) and low level light therapy (LLLT). © 2016 Journal of Biomedical Photonics & Engineering.

Keywords: tissue optics, photothermal effects, nonlinear interactions, temperature, tissue damage, photoacoustics, acoustooptics, sonoluminescence, Raman scattering, multiphoton autofluorescence, SHG, terahertz, photochemical processes, PDT, LLLT.

Paper #3042 received 2016.05.17; accepted for publication 2016.09.10; published online 2016.09.30.
[doi: 10.18287/JBPE16.02.030201](https://doi.org/10.18287/JBPE16.02.030201)

References

1. V. V. Tuchin, "Tissue optics and photonics: Biological tissue structures," *J. of Biomedical Photonics & Eng.* 1(1), 3–21 (2015).
2. V. V. Tuchin, "Tissue optics and photonics: Light-tissue interaction," *J. of Biomedical Photonics & Eng.* 1(2), 98–135 (2015).
3. V. S. Letokhov, "Laser biology and medicine," *Nature* 316 (6026) 325–328 (1985).
4. G. J. Müller, and D. H. Sliney (eds.), *Dosimetry of Laser Radiation in Medicine and Biology*, SPIE Inst. Adv. Opt. Techn. IS5, SPIE Press, Bellingham, WA (1989).
5. D. H. Sliney, and S. L. Trokel, *Medical Lasers and their Safe Use*, Academic Press, Inc., New York, et al. (1993).
6. A. Katzir, *Lasers and Optical Fibers in Medicine*, Academic Press, Inc., San Diego, et al. (1993).
7. V. V. Tuchin (ed.), *Selected Papers on Tissue Optics: Applications in Medical Diagnostics and Therapy*, MS102, SPIE Press, Bellingham, WA (1994).
8. G. Müller, and A. Roggan (eds.), *Laser-Induced Interstitial Thermotherapy*, SPIE Press Bellingham, WA (1995).
9. H.-P. Berlien, and G.J. Müller (eds.), *Applied Laser Medicine*, Springer-Verlag, Berlin (2003).
10. M. H. Niemz, *Laser-Tissue Interactions: Fundamentals and Applications*, 3rd ed., Springer, Berlin, Heidelberg, New York (2007).
11. R. Splinter, and B.A. Hooper, *An Introduction to Biomedical Optics*, CRC Press, Taylor & Francis Group, NY, London (2007).
12. L. Pavesi, Ph. M. Fauchet (eds.), *Biophotonics*, Springer Verlag, Berlin, Heidelberg (2008).
13. E. D. Baron (ed.), *Light-Based Therapies for Skin of Color*, Springer, London (2009).
14. G. Ahluwalia (ed.), *Light Based Systems for Cosmetic Application*, William Andrew, Norwich (2009).

15. V. V. Tuchin, *Lasers and Fibre Optics in Biomedical Science*, 2nd ed., Fizmatlit, Moscow (2010).
16. F.S. Pavone (ed.), *Laser Imaging and Manipulation in Cell Biology*, Wiley-VCH Verlag GmbH & Co. KGaA, Weinheim (2010).
17. L. A. Dombrovsky, and D. Baillis, *Thermal Radiation in Disperse Systems: An Engineering Approach*, Begell House, New York (2010).
18. A. J. Welch, and M. J. C. van Gemert (eds.), *Optical-Thermal Response of Laser-Irradiated Tissue*, 2nd ed., Springer Science+Business Media, Berlin, Heidelberg, New York (2011).
19. D. A. Boas, C. Pitris, and N. Ramanujam (eds.), *Handbook of Biomedical Optics*, CRC Press, Taylor & Francis Group, London (2011).
20. J. Popp, V. V. Tuchin, A. Chiou, and S. H. Heinemann (eds.), *Handbook of Biophotonics*, vol. 1: Basics and Techniques, Wiley-VCH Verlag GmbH & Co. KGaA, Weinheim (2011).
21. J. Popp, V. V. Tuchin, A. Chiou, and S. H. Heinemann (eds.), *Handbook of Biophotonics*, vol. 2: Photonics for Health Care, Wiley-VCH Verlag GmbH & Co. KGaA, Weinheim (2012).
22. J. Popp, V. V. Tuchin, A. Chiou, and S. H. Heinemann (eds.), *Handbook of Biophotonics*, vol. 3: Photonics in Pharmaceuticals, Bioanalysis and Environmental Research, Wiley-VCH Verlag GmbH & Co. KGaA, Weinheim (2012).
23. V. V. Tuchin, *Dictionary of Biomedical Optics and Biophotonics*, SPIE Press, Bellingham, WA (2012).
24. H. Jelinkova (ed.), *Lasers for Medical Applications: Diagnostics, Therapy and Surgery*, Woodhead Publishing, Ltd., Cambridge (2013).
25. R. Liang (ed.), *Biomedical Optical Imaging Technologies. Design and Applications*, Springer-Verlag, Berlin, Heidelberg (2013).
26. T. Vo-Dinh (ed.), *Biomedical Photonics Handbook*, vol. 1: Fundamentals, devices, and techniques, vol. 2: Biomedical diagnostics, vol. 3: Therapeutics and advanced biophotonics, 2nd ed., CRC Press, Boca Raton (2015).
27. F. S. Pavone, and P. J. Campagnola (eds.), *Second Harmonic Generation Imaging*, CRC Press, Taylor & Francis Group, Boca Raton, London, New York (2014).
28. K. Kulikov, *Laser Interaction with Biological Material. Mathematical Modeling*, Springer, Cham, Heidelberg, New York, Dordrecht, London (2014).
29. V. V. Tuchin, *Tissue Optics: Light Scattering Methods and Instruments for Medical Diagnostics*, 3rd ed., PM 254, SPIE Press, Bellingham, WA (2015).
30. B. Querleux (ed.), *Computational Biophysics of the Skin*, CRC Press, Taylor & Francis Group, London (2015).
31. F. D. Dip, T. Ishizawa, N. Kokudo, and R. Rosenthal (eds.), *Fluorescence Imaging for Surgeons: Concepts and Applications*, Springer Science + Business Media, New York (2015).
32. V. V. Tuchin (ed.), *Handbook of Optical Biomedical Diagnostics. Vol. 1: Light–Tissue Interaction*, 2nd ed., PM262, SPIE Press, Bellingham, WA (2016).
33. V. V. Tuchin (ed.), *Handbook of Optical Biomedical Diagnostics. Vol. 2: Methods*, 2nd ed., PM263, SPIE Press, Bellingham, WA (2016).
34. I. J. Bigio, and S. Fantini, *Quantitative Biomedical Optics: Theory, Methods, and Applications*, Cambridge University Press, Cambridge (2016).
35. C. H. G. Wright, S. F. Barrett, and A. J. Welch, “[Laser-tissue interaction](#)” in *Lasers in Medicine*, D. R. Vij and K. Mahesh (eds.), Kluwer Academic Publishers, Boston, Dordrecht, London, 21–58 (2002).
36. A. Vogel, and V. Venugopalan, “[Mechanisms of pulsed laser ablation of biological tissues](#),” *Chem. Rev.* 103, 577–644 (2003); Erratum, *Chem. Rev.* 103, 2079 (2003).
37. A. Vogel, J. Noack, G. Hüttman, G. Paltauf, “[Mechanisms of femtosecond laser nanosurgery of cells and tissues](#),” *Appl. Phys. B: Lasers Opt.* 81, 1015–1047 (2005).
38. S. L. Jacques, “[Ratio of entropy to enthalpy in thermal transitions in biological tissues](#),” *J. Biomed. Opt.* 11(4), 041108 (2006).
39. J. A. Pearce, “[Improving accuracy in Arrhenius models of cell death: Adding a temperature-dependent time delay](#),” *J. Biomech. Eng.* 137(12), 121006 (2015).
40. I. A. Lubashevsky, A. V. Priezhev, V. V. Gafiychuk, and M. G. Cadjan, “[Local thermal coagulation due to laser-tissue interaction as irreversible phase transition](#),” *J. Biomed. Opt.* 2(1), 95–105 (1997).
41. Yu. N. Scherbakov, A. N. Yakunin, I. V. Yaroslavsky, and V. V. Tuchin, “Thermal process modeling during uncoagulating laser radiation interaction with multi-layer biotissue. 1. Theory and calculating models,” *Opt. Spectroscopy* 76(5), 754–758 (1994).
42. Yu. N. Scherbakov, A. N. Yakunin, I. V. Yaroslavsky, and V. V. Tuchin, “Thermal process modeling during uncoagulating laser radiation interaction with multi-layer biotissue. 2. Numerical results,” *Opt. Spectroscopy* 76(5), 759–765 (1994).

43. V. V. Tuchin, Yu. N. Scherbakov, A. N. Yakunin, and I. V. Yaroslavsky, "Numerical technique for modeling of laser-induced hyperthermia," in *Laser-Induced Interstitial Thermotherapy*, G. Müller, and A. Roggan (eds.), SPIE Press, Bellingham, Washington, 100–113 (1995).
44. I. V. Yaroslavsky, J. J. Childs, Jr., M. Z. Smirnov, A. V. Erofeev, and G. B. Altschuler, "Self-adaptation optical effects in photothermal treatment of skin structures," *IEEE J. Select. Tops Quant. Electr.* 20(2), 7101109 (2014).
45. L. A. Dombrovsky, J. H. Randrianalisoa, W. Lipinski, and V. Timchenko, "Simplified approaches to radiative transfer simulations in laser induced hyperthermia of superficial tumors," *Comput. Therm. Sci.* 5(6), 521–530 (2013).
46. M. Jasiński, E. Majchrzak, and L. Turchan, "Numerical analysis of the interactions between laser and soft tissues using generalized dual-phase lag equation," *Appl. Math. Model.* 40(2), 750–762 (2016).
47. L. Lévesque, J.-M. Noël, and C. Scott, "Controlling the temperature of bones using pulsed CO₂ lasers: observations and mathematical modeling," *Biomed. Opt. Express* 6(12) 4768–4780 (2015).
48. A. Klinger, L. Krapf, R. Orzekowsky-Schroeder, N. Koop, A. Vogel, and G. Hüttmann, "Intravital autofluorescence 2-photon microscopy of murine intestinal mucosa with ultra-broadband femtosecond laser pulse excitation: image quality, photodamage, and inflammation," *J. Biomed. Opt.* 20(11), 116001 (2015).
49. A. N. Yakunin, Y. A. Avetisyan, and V. V. Tuchin, "Quantification of laser local hyperthermia induced by gold plasmonic nanoparticles," *J. Biomed. Opt.*, 20(5), 051030 (2015).
50. A. Rosenwaig, *Photoacoustics and Photoacoustic Spectroscopy*, Wiley, New York (1983).
51. A. V. Priezzhev, V. V. Tuchin, and L. P. Shubochkin, *Laser Diagnostics in Biology and Medicine*, Nauka, Moscow (1989).
52. V. P. Zharov, and V. S. Letokhov, *Laser Opto-Acoustic Spectroscopy*, Springer Verlag, New York (1989).
53. V. E. Gusev, and A. A. Karabutov, *Laser Photoacoustics*, AIP Press, New York (1993).
54. S. E. Braslavsky, and K. Heihoff, "Photothermal methods" in *Handbook of Organic Photochemistry*, J. C. Scaiano (ed.), CRC Press, Boca Raton (1989).
55. A. Mandelis, and P. Hess (eds.), *Progress in Photothermal and Photoacoustic Science and Technology. Life and Earth Sciences*, SPIE Press, Bellingham, WA (1997).
56. V. Ntziachristos, J. Ripoll, L. V. Wang, and R. Weissleder, "Looking and listening to light: The revolution of photonic imaging," *Nature Biotechnol.* 23(3), 313–320 (2005).
57. L. V. Wang, and H.-I. Wu, *Biomedical Optics: Principles and Imaging*, Wiley-Interscience, Hoboken, New Jersey (2007).
58. L. Wang (ed.), *Photoacoustic Imaging and Spectroscopy*, CRC Press, Taylor & Francis Group, London (2009).
59. R. Myllylä, Z. Zhao, and M. Kinnunen, "Pulsed photoacoustic techniques and glucose determination in human blood and tissue," in *Handbook of Optical Sensing of Glucose in Biological Fluids and Tissues*, V. V. Tuchin (ed.), CRC Press, Taylor & Francis Group, London, 419–455 (2009).
60. S. Hu, K. Maslov, and L. V. Wang, "Optical-resolution photoacoustic microscopy for in vivo volumetric microvascular imaging in intact tissues" in *Handbook of Photonics for Biomedical Science*, V. V. Tuchin (ed.), CRC Press, Taylor & Francis Group, London, 361–375 (2010).
61. T. Khokhlova, I. Pelivanov, and A. Karabutov, "Advances in optoacoustic imaging," in *Handbook of Photonics for Biomedical Science*, V. V. Tuchin (ed.), CRC Press, Taylor & Francis Group, London, 343–360 (2010).
62. V. Ntziachristos, and D. Razansky, "Molecular imaging by means of multispectral optoacoustic tomography (MSOT)," *Chem. Rev.* 110, 2783–2794 (2010).
63. V. V. Tuchin, E. I. Galanzha, and V. P. Zharov, "In vivo photothermal and photoacoustic flow cytometry," in *Advanced Optical Cytometry: Methods and Disease Diagnoses*, V. V. Tuchin (ed.), Wiley-VCH Verlag GmbH & Co. KGaA, Weinheim, 501–571 (2011).
64. V. V. Tuchin, A. Tárnok, and V. P. Zharov, "In vivo flow cytometry: A horizon of opportunities," *Cytometry A* 79A(10), 737–745 (2011).
65. R. O. Esenaliev, "Biomedical optoacoustics," *J. Innov. Opt. Health Sci.* 4(1), 39–44 (2011).
66. L. V. Wang, and S. Hu, "Photoacoustic tomography: In vivo imaging from organelles to organs," *Science* 335(6075), 1458–1462 (2012).
67. A. Taruttis, and V. Ntziachristos, "Optoacoustic molecular imaging: Methods and applications," in *Advanced Biophotonics: Tissue Optical Sectioning*, R. K. Wang, and V. V. Tuchin (eds.), CRC Press, Taylor & Francis Group, London, 449–474 (2013).
68. V. V. Tuchin, "In vivo optical flow cytometry and cell imaging," *Rivista Del Nuovo Cimento*, 37(7), 375–416 (2014).
69. B. Li, B. Majaron, J. A. Viator, T. E. Milner, Z. Chen, Y. Zhao, H. Ren, and J. S. Nelson, "Accurate measurement of blood vessel depth in port wine stained human skin in vivo using pulsed photothermal radiometry," *J. Biomed. Opt.* 9(5), 961–966 (2004).

70. R. J. Jeon, A. Mandelis, V. Sanchez, and S. H. Abrams, “Noninvasive, noncontacting frequency-domain photothermal radiometry and luminescence depth profilometry of carious and artificial subsurface lesions in human teeth,” *J. Biomed. Opt.* 9(4), 804–819 (2004).
71. J. A. Garcia, A. Mandelis, S. H. Abrams, and A. Matvienko, “Photothermal radiometry and modulated luminescence: Applications for dental caries detection” in *Handbook of Biophotonics 2: Photonics for Health Care*, J. Popp, V. V. Tuchin, A. Chiou, and S. H. Heinemann (eds.), Wiley-VCH Verlag GmbH & Co. KGaA, Weinheim, 1047–1052 (2012).
72. V. P. Zharov, E. I. Galanzha, and V. V. Tuchin, “Integrated photothermal flow cytometry in vivo,” *J. Biomed. Opt.* 10, 051502-1–13 (2005).
73. V. P. Zharov, E. I. Galanzha, and V. V. Tuchin, “Photothermal image flow cytometry in vivo,” *Opt. Lett.* 30(6), 628–630 (2005).
74. D. A. Nedosekin, E. I. Galanzha, E. Dervishi, A. S. Biris, and V. P. Zharov, “Super-resolution nonlinear photothermal microscopy,” *Small* 10(1), 135–142 (2014).
75. K. Maslov, G. Stoica, and L. V. Wang, “In vivo dark-field reflection-mode photoacoustic microscopy,” *Opt. Lett.* 30(6), 625–627 (2005).
76. A. A. Karabutov, and A.A. Oraevsky, “Time-resolved detection of optoacoustic profiles for measurement of optical energy distribution in tissues,” in *Handbook of Optical Biomedical Diagnostics*, V. V. Tuchin (ed.), SPIE Press, Bellingham, Washington, 585–674 (2002).
77. A. A. Oraevsky, and A. A. Karabutov, “Optoacoustic tomography” in *Biomedical Photonics Handbook*, T. Vo-Dinh (ed.), CRC Press, Boca Raton, 34-1–34 (2003).
78. I. M. Pelivanov, A. A. Karabutov, T. D. Khokhlova, and A. A. Oraevsky, “Measurement of optical fluence distribution and optical properties of tissues using time-resolved profiles of optoacoustic pressure” in *Handbook of Optical Biomedical Diagnostics. Vol. 1: Light–Tissue Interaction*, V. V. Tuchin (ed.), 2nd ed., PM262, SPIE Press, Bellingham, WA (2016).
79. H. Fang, K. Maslov, and L. V. Wang, “Photoacoustic Doppler effect from flowing small light-absorbing particles,” *Phys. Rev. Lett.* 99, 184501 (2007).
80. X. Xu, H. Liu, and L. V. Wang, “Time-reversed ultrasonically encoded optical focusing into scattering media,” *Nature Photon.* 5, 154–157 (2011).
81. M. Kempe, M. Larionov, D. Zaslavsky, and A. Z. Genack, “Acousto-optic tomography with multiply scattered light,” *J. Opt. Soc. Am. A* 14(5), 1151–1158 (1997).
82. L. V. Wang, “Mechanisms of ultrasonic modulation of multiply scattered coherent light: An analytical mode,” *Phys. Rev. Lett.* 87, 043903 (2001).
83. J. R. Lakowicz, *Principles of Fluorescence Spectroscopy*, 3rd ed., Springer, New York (2006).
84. B. B. Das, F. Liu, and R. R. Alfano, “Time-resolved fluorescence and photon migration studies in biomedical and random media,” *Rep. Prog. Phys.* 60, 227–292 (1997).
85. A. Kishen, and A. Asundi (eds.), *Photonics in Dentistry. Series of Biomaterials and Bioengineering*, Imperial College Press, London (2006).
86. D. L. Andrews (ed.), *Encyclopedia of Applied Spectroscopy*, Wiley-VCH Verlag GmbH & Co. KGaA, Weinheim (2009).
87. J. T. Alander, I. Kaartinen, A. Laakso, T. Pätälä, T. Spillmann, V. V. Tuchin, M. Venermo, P. Välisuo, ”A review of indocyanine green fluorescent imaging in surgery,” *Int. J. Biomed. Imaging* 2012, 940585 (2012).
88. J. T. Alander, O. M. Villet, T. Pätälä, I. S. Kaartinen, M. Lehecka, T. Nakaguchi, T. Suzuki, and V. Tuchin, “Review of indocyanine green imaging in surgery” in *Fluorescence Imaging for Surgeons: Concepts and Applications*, F. D. Dip, T. Ishizawa, N. Kokudo, R. Rosenthal (eds.), Springer International Publishing Switzerland, Cham, Heidelberg, New York, Dordrecht, London, 35–53 (2015).
89. A. Mazhar, D. Cuccia, S. Gioux, A. Durkin, J. Frangioni, and B. Tromberg, “Structured illumination enhances resolution and contrast in thick tissue fluorescence imaging,” *J. Biomed. Opt.* 15(1), 010506 (2010).
90. R. B. Saager, D. J. Cuccia, S. Saggese, K. M. Kelly, and A. J. Durkin, “Quantitative fluorescence imaging of protoporphyrin IX through determination of tissue optical properties in the spatial frequency domain,” *J. Biomed. Opt.* 16(12), 126013 (2011).
91. Yu. P. Sinichkin, N. Kollias, G. I. Zonios, S. R. Utz, and V. V. Tuchin, “Reflectance and fluorescence spectroscopy of human skin in vivo” in *Handbook of Optical Biomedical Diagnostics. Vol. 2: Methods*, V. V. Tuchin (ed.), 2nd ed., PM263, SPIE Press, Bellingham, WA, 99–190 (2016).
92. H. Schneckenburger, W. S. L. Strauss, K. Stock, and R. Steiner, “Fluorescence technologies in biomedical diagnostics” in *Handbook of Optical Biomedical Diagnostics. Vol. 2: Methods*, V. V. Tuchin (ed.), 2nd ed., PM263, SPIE Press, Bellingham, WA, 241–304 (2016).
93. A. N. Yaroslavsky, E. V. Salomatina, V. Neel, R. Anderson, and T. Flotte, “Fluorescence polarization of tetracycline derivatives as a technique for mapping nonmelanoma skin cancers,” *J. Biomed. Opt.* 12(1), 014005 (2007).

94. A. N. Yaroslavsky, R. Patel, E. Salomatina, C. Li, C. Lin, M. Al-Arashi, and V. Neel, “[High-contrast mapping of basal cell carcinomas](#),” *Opt. Lett.* 37(4), 644–646 (2012).
95. J. Soni, H. Purwar, H. Lakhota, S. Chandel, C. Banerjee, U. Kumar, and N. Ghosh, “[Quantitative fluorescence and elastic scattering tissue polarimetry using an Eigenvalue calibrated spectroscopic Mueller matrix system](#),” *Opt. Express* 21(13), 15475–15489 (2013).
96. J. Jagtap, S. Chandel, N. Das, J. Soni, S. Chatterjee, A. Pradhan, and N. Ghosh, “[Quantitative Mueller matrix fluorescence spectroscopy for precancer detection](#),” *Opt. Lett.* 39(2), 243–246 (2014).
97. V. V. Tuchin, “[Polarized light interaction with tissues: a tutorial](#),” *J. Biomed. Opt.* 21(7), 071114 (2016).
98. W. Denk, “[Two-photon excitation in functional biological imaging](#),” *J. Biomed. Opt.* 1(3), 296–304 (1996).
99. A. Diaspro (ed.), *Confocal and Two-Photon Microscopy: Foundations, Applications, and Advances*, Wiley-Liss, New York (2002).
100. W. R. Zipfel, R. M. Williams, and W. W. Webb, “[Nonlinear magic: multiphoton microscopy in the bioscience](#),” *Nature Biotechnol.* 21, 1369–1377 (2003).
101. B. R. Masters, and P. T. C. So (eds.), *Handbook of Biomedical Nonlinear Optical Microscopy*, Oxford University Press, New York (2008).
102. M. Gu, D. Bird, D. Day, L. Fu, and D. Morrish, *Femtosecond Biophotonics. Core Technology and Applications*, Cambridge University Press, New York (2010).
103. K. König, and A. Uchugonova, “[Multiphoton imaging and nanoprocessing of human stem cells](#)” in *Laser Imaging and Manipulation in Cell Biology*, F. S. Pavone (ed.), Wiley-VCH Verlag GmbH & Co. KGaA, Weinheim, 7–34 (2010).
104. Q. Shen, and L. V. Wang, “[Two-dimensional imaging of dense tissue simulating turbid media by use of sonoluminescence](#),” *Appl. Opt.* 38(1), 246–252 (1999).
105. P. J. Campagnola, H. A. Clark, W. A. Mohler, A. Lewis, and L. M. Loew, “[Second-harmonic imaging microscopy of living cells](#),” *J. Biomed. Opt.* 6(3), 277–286 (2001).
106. A. T. Tu, *Raman Spectroscopy in Biology*, John Wiley & Sons Ltd., New York (1982).
107. A. Mahadevan–Jansen, and R. Richards-Kortum, “[Raman spectroscopy for detection of cancers and precancers](#),” *J. Biomed. Opt.* 1(1), 31–70 (1996).
108. G. J. Puppels, “[Confocal Raman Microspectroscopy](#)” in *Fluorescent and Luminescent Probes for Biological Activity*, W. Mason (ed.), Academic Press, London., 377–406 (1999).
109. J. M. Chalmers, and P. R. Griffiths (eds.), *Handbook of Vibrational Spectroscopy*, John Wiley & Sons, Chichester (2002).
110. J. Popp, and M. Strehle (eds.), *Biophotonics: Visions for Better Health Care*, Wiley-VCH Verlag GmbH & Co. KGaA, Weinheim (2006).
111. S. Rehman, I. ur Rehman, and Z. Movasaghi, *Vibrational Spectroscopy for Tissue Analysis*, CRC Press, Taylor & Francis Group, Boca Raton, FL (2013).
112. Y. Ozaki, A. Ikehata, and H. Shinzawa, “[Near-Infrared Spectroscopy in Biological Molecules and Tissues](#)” in *Encyclopedia of Biophysics*, G. C. K. Roberts (ed.), Springer-Verlag, Berlin, Heidelberg, 1695–1706 (2013).
113. Y. Kitahama, T. Itoh, P. Pienpinijtham, S. Ekgasit, X. X. Han, and Y. Ozaki, “[Biological applications of SERS using functional nanoparticles](#),” *ACS Symp Ser (Am. Chem. Soc.)*, 1113, 181–234 (2012).
114. G. W. Lucassen, P. J. Caspers, G. J. Puppels, M. E. Darwin, and J. Lademann, “[Infrared and Raman spectroscopy of human skin in vivo](#),” in *Handbook of Optical Biomedical Diagnostics. Vol. 2: Methods*, V. V. Tuchin (ed.), 2nd ed., PM263, SPIE Press, Bellingham, WA, 191–210 (2016).
115. U. Utzinger, D. L. Heintselman, A. Mahadevan-Jansen, A. Malpica, M. Follen, and R. Richards-Kortum, “[Near-infrared Raman spectroscopy for in vivo detection of cervical precancers](#),” *Appl. Spectrosc.* 55, 955–959 (2001).
116. R. Petry, M. Schmitt, and J. Popp, “[Raman spectroscopy—A prospective tool in the life sciences](#),” *Chemphyschem.* 4, 14–30 (2003).
117. C. Krafft, B. Dietzek, M. Schmitt, and J. Popp, “[Raman and coherent anti-Stokes Raman scattering microspectroscopy for biomedical applications](#),” *J. Biomed. Opt.* 17(4), 040801 (2012).
118. M. M. Nazarov, A. P. Shkurinov, V. V. Tuchin, and X.-C. Zhang, “[Terahertz tissue spectroscopy and imaging](#)” in *Handbook of Photonics for Biomedical Science*, V. V. Tuchin (ed.), CRC Press, Taylor & Francis Group, London, 591–617 (2010).
119. X.-C. Zhang, and J. Xu, *Introduction to THz Wave Photonics*, Springer, New York (2010).
120. A. A. Angeluts, A. V. Balakin, M. G. Evdokimov, M. N. Esaulkov, M. M. Nazarov, I. A. Ozheredov, D. A. Sapozhnikov, P. M. Solyankin, O. P. Cherkasova, and A. P. Shkurinov, “[Characteristic responses of biological and nanoscale systems in the terahertz frequency range](#),” *Quant. Electron.*, 44(7) 614–632 (2014).
121. G. J. Wilmint, and J. E. Grundt, “[Invited review article: Current state of research on biological effects of terahertz radiation](#),” *J. Infrared Milli. Terahz Waves* 32, 1074–1122 (2011).

122. C. S. Joseph, R. Patel, V. A. Neel, R. H. Giles, and A. N. Yaroslavsky, "Imaging of ex vivo nonmelanoma skin cancers in the optical and terahertz spectral regions. Optical and Terahertz skin cancers imaging," *J. Biophoton.* 7, 295–303 (2014).
123. M. M. Nazarov, A. P. Shkurinov, E. A. Kuleshov, and V. V. Tuchin, "Terahertz time-domain spectroscopy of biological tissues," *Quant. Electr.* 38(7) 647–654 (2008).
124. A. S. Kolesnikov, E. A. Kolesnikova, K. N. Kolesnikova, D. K. Tuchina, A. P. Popov, A. A. Skaptsov, M. M. Nazarov, A. P. Shkurinov, A. G. Terentyuk, and V. V. Tuchin, "THz monitoring of the dehydration of biological tissues affected by hyperosmotic agents," *Phys. Wave Phenom.* 22(3), 169–176 (2014).
125. T. I. Karu, *Photobiology of Low-Power Laser Therapy*, Harwood Academic Publ., Chur et al. (1989).
126. T. I. Karu, "Mitochondrial signaling in mammalian cells activated by red and near-IR radiation," *Photochem. Photobiol.* 84, 1091–1099 (2008).
127. B. W. Henderson, and T.J. Dougherty (eds.), *Photodynamic Therapy: Basic Principles and Clinical Applications*, Marcel-Dekker, New York (1992).
128. W. L. Morison, *Phototherapy and Photochemotherapy of Skin Disease*, 3rd ed., Taylor and Francis, New York (2005).
129. M. Hamblin, and P. Mroz (eds.), *Advances in Photodynamic Therapy: Basic, Translational and Clinical*, Artec House, Boston, London (2008).
130. B. C. Wilson, "Photodynamic therapy/diagnostics: Principles, practice and advances" in *Handbook of Photonics for Biomedical Science*, V. V. Tuchin (ed.), CRC Press, Taylor & Francis Group, London, 649–686 (2010).
131. M. L. T. Elsaie, *Photodynamic Therapy. New Research*, Nova Science Publishers, Inc., New York (2013).
132. M. H. Abdel-Kader (ed.), *Photodynamic Therapy. From Theory to Application*, Springer-Verlag, Berlin, Heidelberg (2014).
133. Y.-Y. Huang, A. C.-H. Chen, and M. R. Hamblin, "Advances in low-intensity laser and phototherapy" in *Handbook of Photonics for Biomedical Science*, V. V. Tuchin (ed.), CRC Press, Taylor & Francis Group, London, 687–716 (2010).
134. Y.-Y. Huang, M. R. Hamblin, and L. De Taboada, "Low-level laser therapy in stroke and central nervous system" in *Handbook of Photonics for Biomedical Science*, V. V. Tuchin (ed.), CRC Press, Taylor & Francis Group, London, 717–737 (2010).
135. S. Kim, S. Shin, and S. Jeong, "Effects of tissue water content on the propagation of laser light during low-level laser therapy," *J. Biomed. Opt.* 20(5), 051027 (2015).
136. P. J. Verveer (ed.), *Advanced Fluorescence Microscopy Methods and Protocols*, Humana Press, Springer Science+Business Media, New York (2015).
137. G. Olivi, R. De Moor, and E. DiVito (eds.), *Lasers in Endodontics. Scientific Background and Clinical Applications*, Springer International Publishing Switzerland, Cham, Heidelberg, New York, Dordrecht, London (2016).
138. A. Kyagova, A. Potapenko, M. Möller, H. Stopper, and W. Adam, "Photohemolysis sensitized by the Furocoumarin derivative Alloimperatorin and its hydroperoxide photooxidation product," *Photochem. Photobiol.* 90, 162–170 (2014).
139. A. A. Krasnovsky Jr., "Singlet oxygen and primary mechanisms of photodynamic therapy and photodynamic diseases" in *Photodynamic therapy at the cellular level*, A. B. Uzdensky (ed.), Research Signpost, Trivandrum-695 023, Kerala, India, 17-62 (2007).
140. A. A. Krasnovsky Jr., A. S. Kozlov, Y. V. Roumbal, "Photochemical investigation of the IR absorption bands of molecular oxygen in organic and aqueous environment," *Photochem. Photobiol. Sci.* 11, 988–997 (2012).
141. S. G. Sokolovski, S. A. Zolotovskaya, A. Goltsov, C. Pourreyron, A. P. South, and E. U. Rafailov, "Infrared laser pulse triggers increased singlet oxygen production in tumour cells," *Sci. Rep.* 3, 3484 (2013).
142. P. Woodgate, and L. A. Jardine, "Neonatal jaundice: phototherapy," *BMJ Clin. Evid.* 2015, 0319 (2015).
143. E. A. Genina, A. N. Bashkatov, and V. V. Tuchin, "Study of diffusion of indocyanine green as a photodynamic dye into skin using backscattering spectroscopy," *Quant. Electr.* 44 (7) 689–695 (2014).
144. G. Terentyuk, E. Panfilova, V. Khanadeev, D. Chumakov, E. Genina, A. Bashkatov, V. Tuchin, A. Bucharskaya, G. Maslyakova, N. Khlebtsov, and B. Khlebtsov, "Gold nanorods with hematoporphyrin-loaded silica shell for dual-modality photodynamic and photothermal treatment of tumors in vivo," *Nano Research.* 7(3), 325–337 (2014).
145. B. N. Khlebtsov, E. S. Tuchina, V. A. Khanadeev, E. V. Panfilova, P. O. Petrov, V. V. Tuchin, and N. G. Khlebtsov, "Enhanced photoinactivation of *Staphylococcus aureus* with nanocomposites containing plasmonic particles and hematoporphyrin," *J. Biophoton.* 6(4), 338–351 (2013).
146. E. S. Tuchina, V. V. Tuchin, B. N. Khlebtsov, and N. G. Khlebtsov, "Phototoxic effect of conjugates of plasmon-resonance nanoparticles with indocyanine green dye on *Staphylococcus aureus* induced by IR laser radiation," *Quant. Electr.* 41(4) 354–359 (2011).

147. I. Yu. Yanina, V. A. Bochko, J. T. Alander, and V. V. Tuchin, "Optical image analysis of fat cells for indocyanine green mediated near-infrared laser treatment," *Laser Phys. Lett.* 8(9), 684–690 (2011).
148. I. Yu. Yanina, V. V. Tuchin, N. A. Navolokin, O. V. Matveeva, A. B. Bucharskaya, G. N. Maslyakova, and G. B. Altshuler, "Fat tissue histological study at indocyanine green-mediated photothermal/photodynamic treatment of the skin in vivo," *J. Biomed. Opt.* 17 (5), 058002 (2012).
149. I. Yu. Yanina, N. A. Trunina, and V. V. Tuchin, "Optical coherence tomography of adipose tissue at photodynamic/photothermal treatment in vitro," *J. Innovative Opt. Health Sci.* 6 (2) 1350010 (2013).
150. E. A. Genina, A. N. Bashkatov, and V. V. Tuchin, "Effect of ethanol on the transport of methylene blue through stratum corneum," *Med. Laser Appl.* 23, 31–38 (2008).
151. Yu. A. Vladimirov and A. Ya. Potapenko, *Physico-Chemical Basis of Photobiological Processes*, the textbook for high schools, 2nd ed., Moscow, Drofa (2006).
152. A. A. Potapov, S. A. Goryaynov, V. A. Okhlopkov, L. V. Shishkina, V. B. Loschenov, T. A. Savelieva, D. A. Golbin, A. P. Chumakova, M. F. Goldberg, M. D. Varyukhina, and A. Spallone, "Laser biospectroscopy and 5-ALA fluorescence navigation as a helpful tool in the meningioma resection," *Neurosurg. Rev.* 39(3), 437–447 (2016).
153. B. Khlebtsov, E. Tuchina, V. Tuchin, and N. Khlebtsov, "Multifunctional Au nanoclusters for targeted bioimaging and enhanced photodynamic inactivation of *Staphylococcus aureus*," *RSC Advances* 5, 61639–61649 (2015).
154. A. V. Priezzhev, H. Schneckenburger, and V. V. Tuchin, "Special Section Guest Editorial: Laser Applications in Life Sciences," *J. Biomed. Opt.* 20 (5), 051001 (2015).
155. ANSI Z136.3-2005, ANSI, American National Standard for the Safe Use of Lasers in Health Care Facilities, Laser Institute of America, Orlando, FL (2005).
156. ANSI Z136.1-2007, ANSI, American National Standard for the Safe Use of Lasers, Laser Institute of America, Orlando, FL (2007).
157. E. A. Genina, V. A. Titorenko, A. V. Belikov, A. N. Bashkatov, and V. V. Tuchin, "Adjunctive dental therapy via tooth plaque reduction and gingivitis treatment by blue light-emitting diodes tooth brushing," *J. Biomed. Opt.* 20(12) 128004 (2015).
158. T. I. Karu, L. V. Pyatibrat, and N. I. Afanasyeva, "Cellular effects of low power laser therapy can be mediated by nitric oxide," *Lasers Surg. Med.* 36, 307–314 (2005).
159. E. Tuchina, and V. Tuchin, "Low-intensity LED (625 and 405 nm) and laser (805 nm) killing of *Propionibacterium acnes* and *Staphylococcus epidermidis*," *Proc. SPIE* 7165, 71650I (2009).
160. G. Popescu, *Quantitative Phase Imaging of Cells and Tissues*, McGraw-Hill, NY (2011).
161. V. V. Tuchin (ed.), *Coherent-Domain Optical Methods: Biomedical Diagnostics, Environmental Monitoring and Material Science*, Berlin, Heidelberg, N. Y., Springer-Verlag, 2nd ed., 2 vols. (2013).
162. W. Drexler, and J. G. Fujimoto (eds.), *Optical Coherence Tomography: Technology and Applications*, 2nd ed., Springer Reference, Science + Business Media, New York (2015).

Contents

1 Introduction	3.3.3 Low-coherent light interferometry – optical coherence tomography
2 Biological tissue structures	3.4 Dynamic light scattering
2.1 General definitions and characteristics	3.4.1 Quasi-elastic light scattering (QELS) and Doppler effect
2.2 Soft tissues	3.4.2 Dynamic speckles
2.3 Hard tissues	3.4.3 Speckle pattern blurring effect – full-field velocity measurements
2.4 Tissue structural anisotropy	3.5 Diffusion wave spectroscopy
2.5 Blood, lymph and other biofluids	3.6 Interaction of the polarized light with tissues
3 Light-tissue interaction: absorption, scattering and polarization	3.6.1 Definitions
3.1 Light reflection and refraction	3.6.2 Single scattering and quasi-ordered tissues
3.2 Light absorption and elastic scattering	3.6.3 Multiple scattering
3.2.1 Absorption and tissue absorbers	3.7 Refractive index and controlling of light interaction with tissues
3.2.2 Scattering – basic definitions	4 Photothermal interactions
3.2.3 Rayleigh scattering	4.1 Temperature rise and tissue damage
3.2.4 Mie scattering	4.2 Photothermal and photoacoustic interactions
3.2.5 Multiple scattering	4.3 Acoustooptical interactions
3.3 Scattering of the coherent light	5 Tissue luminescence, Raman scattering and nonlinear interactions
3.3.1 Random phase screen concept and speckle formation	
3.3.2 Speckle interferometry	

- 5.1 Definitions and one-photon fluorescence
- 5.2 Multiphoton fluorescence
- 5.3 Sonoluminescence
- 5.4 Second harmonic generation
- 5.5 Vibrational energy states excitation and Raman scattering
- 5.6 Terahertz radiation interactions
- 6 Photochemical interactions
 - 6.1 General remarks
 - 6.2 Photodynamic therapy (PDT)
 - 6.3 Low level light therapy (LLLT)
- 7 Conclusion

4 Photothermal interactions

4.1 Temperature rise and tissue damage

When photons traveling in a tissue are absorbed, heat is generated. Generated heat induces several effects in tissue which can be presented in the order of amount of heat deposition: temperature increase and reversible and irreversible alterations in tissue structure [3-47]. The following types of irreversible tissue damage are expected as tissue temperature rises past the critical temperature T_{crit} : *coagulation* (denaturation of cellular and tissue proteins, cell necroses, dehydration; 45–100°C) is the basis for *tissue welding*; *vaporization* (tissue dehydration and vapor bubbles formation (*vacuolization*), $T \geq 100^\circ\text{C}$) is the basis for tissue mechanical destruction; *pyrolysis* ($T \approx 350\text{--}450^\circ\text{C}$) (Fig. 4.1) [4, 5, 15, 18]. For short light pulses, these processes develop as explosion or thermal ablation. All these phenomena are named as photothermal mechanism of tissue damage. During ablation, high pressure is developing in tissue, which can be a reason for shock wave formation and mechanical damage of tissue. This phenomenon is the basis for photomechanical mechanism.

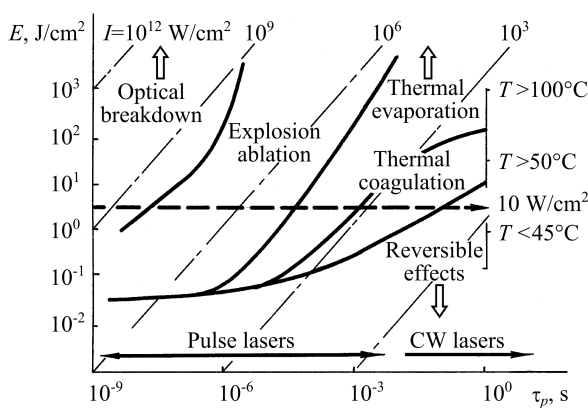


Fig. 4.1 Laser-tissue interaction modes for various energy densities and irradiation times in typical soft tissues (David Sliney’s scheme) (the puncture line corresponds to irradiating dose of $\sim 3 \text{ J/cm}^2$) [4, 5, 15].

The generated heat, described by the heat source term $S(\vec{r})$ at a point \vec{r} , is proportional to the fluence

rate of light $\phi(\vec{r})$ (mW/cm^2) and absorption coefficient $\mu_a(\vec{r})$ in this point

$$S(\vec{r}) = \mu_a(\vec{r})\phi(\vec{r}). \quad (4.1)$$

The traditional *bioheat equation* originated from the energy balance describes the change in tissue temperature over time at point \vec{r} in the tissue

$$\rho c \frac{\partial T(\vec{r}, t)}{\partial t} = \nabla[k_m \nabla T(\vec{r}, t)] + S(\vec{r}) + \rho c w(T_a - T_v), \quad (4.2)$$

where ρ is the tissue mass density (g/cm^3), c is the tissue specific heat ($\text{mJ/g}\cdot^\circ\text{C}$), $T(\vec{r}, t)$ is the tissue temperature ($^\circ\text{C}$) at time t , k_m is the thermal conductivity ($\text{mW/cm}\cdot^\circ\text{C}$), $S(\vec{r})$ is the heat source term (mW/cm^3), w is the tissue blood perfusion rate ($\text{g/cm}^3\cdot\text{s}$), T_a is the inlet arterial temperature ($^\circ\text{C}$), and T_v is the outlet venous temperature ($^\circ\text{C}$), all at point \vec{r} in the tissue. In this equation, convection, radiation, vaporization, and metabolic heat effects are not accounted for because of their negligible effect in many practical cases. The source term is assumed to be stationary over the time interval of heating. The first term to the right of the equal sign describes any heat conduction (typically away from point \vec{r}), and the source term accounts for heat generation due to photon absorption. In most cases of light (laser) tissue interaction, the heat transfer caused by blood perfusion (last term) is negligible.

To solve this equation initial and boundary conditions must be accounted for. The initial condition is the tissue temperature at $t = 0$ and the boundary conditions depend on tissue structure and geometry of light heating. Methods of the *bioheat equation* solving are well developed.

Damage of a tissue is resulted when it is exposed to a high temperature for sufficiently long time interval. The damage function is expressed in terms of an Arrhenius integral [18, 35, 38, 39, 49]:

$$\Omega(\tau) = \ln\left(\frac{C(0)}{C(\tau)}\right) = A \int_0^\tau e^{-\frac{E_a}{RT(t)}} dt, \quad (4.3)$$

where τ is the total heating time (s); $C(0)$ is the original concentration of undamaged tissue; $C(\tau)$ is the remaining concentration of undamaged tissue after time τ ; A is an empirically determined constant (s^{-1}); E_a is an empirically determined activation energy barrier (J/mole); R is the universal gas constant ($8.32 \text{ J/mole}\cdot\text{K}$); and T is the absolute temperature (K).

At noninvasive optical diagnostic and some photochemical applications of light, one has to keep tissue below the damaging temperature so called the critical temperature T_{crit} . This temperature is defined as the temperature for which the damage accumulation rate [18, 35, 38, 39, 49],

$$\frac{d\Omega}{dt} = Ae^{-\frac{E_a}{RT_{crit}}} = 1, \quad (4.4)$$

therefore

$$T_{crit} = \frac{E_a}{R \ln(A)}. \quad (4.5)$$

The constants A and E_a can be calculated from experimental data when tissue is exposed to a constant temperature. For example, for pig skin, $A=3.1 \times 10^{98}$ and $E_a=6.28 \times 10^5$ J/mole, that gives $T_{crit}=332.8$ K or 59.7°C .

With CW light sources due to increasing of the temperature difference between the irradiation and the surrounding tissue, conduction of heat away from the light absorption region into surrounding tissue increases. In dependence of light energy, large tissue volumes may be damaged or losing of heat at the target tissue component may be expected (see Fig. 4.1). For pulsed light little heat is usually lost during the pulse duration since light absorption is a fast process while heat conduction is relatively slow, therefore, more precise tissue damage is possible.

The disadvantage of thermal ablation with CW light sources is undesirable damage to surrounding tissue via its coagulation. Pulsed light can deliver in each pulse a sufficient energy to ablate tissue, but in a short time period for which the tissue is removed before any heat is transferred to the surrounding tissue. To achieve precise tissue cutting, lasers with a very small penetration depth and sharp focusing, like UV excimer ArF laser (193 nm), are used. For cellular precision ablation layer by layer in tissue depth, IR lasers, such as Er: YAG laser (2.79–2.94 μm), CO (5–6.5 μm) and CO₂ (9.2–11.1 μm) lasers are also used.

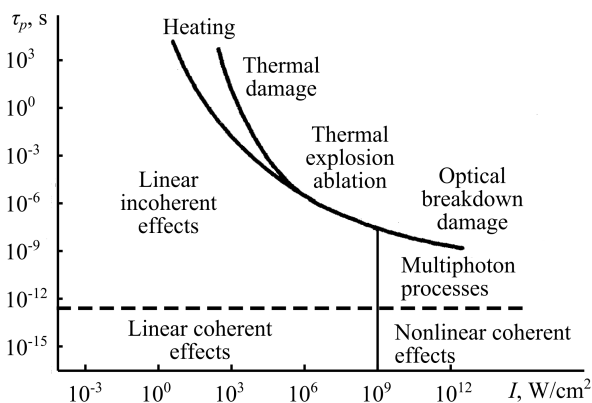


Fig. 4.2 Laser-tissue interaction modes for various energy densities and irradiation times in typical soft tissues (Vladilen Letokhov's scheme) [3, 15].

High-power femtosecond NIR lasers represent a tool for a precise tissue ablation using a nonlinear phenomenon. These lasers emit femtosecond pulse trains with repetition rates from hundreds of MHz to kHz, depending on the laser scheme. When laser pulses

are focused in a tiny volume (typical focus spot in the order of a few microns), very high power densities are reached ($\sim 10^{13}$ W/cm²), which generates free electrons within the focal volume due to nonlinear multiphoton absorption. The free electron density produced by multiphoton ionization may overcome a threshold value for generating an optical breakdown as a consequence of the very fast plasma heating and expansion, thus shock waves and cavitation bubble generation may be observed in tissues [18, 36, 37, 48].

As a condense matter tissue can show any of incoherent or coherent effects at laser irradiation (Fig. 4.2) [3, 15]. Linear incoherent effects exist within a wide area of pulse duration and intensities; for long pulses of 1 s the intensity should not exceed 10 W/cm², for shorter pulses of 10^{-9} s the intensity can be up to 10^9 W/cm². Multiphoton processes may exist at relatively low pulse duration (10^{-9} – 10^{-12} s) at intensities of 10^9 – 10^{12} W/cm² and rather low light energies, not higher 0.1 J/cm². The linear and nonlinear coherent effects may be induced only by a very short pulse with time duration comparable with relaxation time of biological molecules, $\tau \leq 10^{-13}$.

4.2 Photothermal and photoacoustic interactions

The time dependent heat generation in a tissue at interaction with optical radiation is known as optothermal (OT) effect. This interaction also induces a number of thermoelastic effects in a tissue in particular causes generation of acoustic waves [15, 19-23, 26, 29, 32-34, 50-84]. Detection of acoustic waves is a basis for optoacoustic (or photoacoustic) method. The informative features of this method allow one to estimate tissue thermal, optical and acoustical properties which depend on tissue structure peculiarities. Two main modes can be used for excitation of tissue thermal response: 1) a pulse of light excites the sample and the signal is detected in the time domain with a fast by acoustic transducer attached to a wide band amplifier (signal averaging and gating techniques are used to increase the signal-to-noise ratio); 2) an intensity modulated light source is used and the phase sensitive signal detection for the selected modulation frequency is provided.

In every case the thermal waves generated by the heat release result in several effects which have given rise to various techniques: optoacoustics (OA) or photoacoustics (PA), optothermal radiometry (OTR) or photothermal radiometry (PTR), photorefractive techniques, and etc. (Fig. 4.3). When a laser beam falls down to the sample surface and the wavelength is tuned to an absorption line of the tissue component of interest the optical energy is absorbed by the target component and the most of the energy transforms to heat. The time dependent heating leads to all of above mentioned thermal and thermoelastic effects. In OA or PA techniques, a microphone or piezoelectric transducer which are in acoustic contact with the sample are used

as detectors to measure the amplitude or phase of the resultant acoustic wave. In OTR technique, distant IR detectors and array cameras are employed for the sample surface temperature estimation and its imaging.

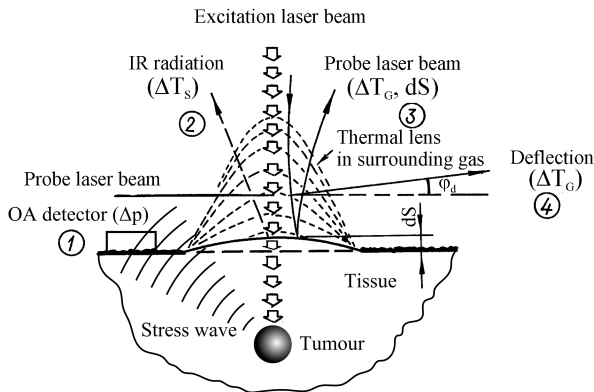


Fig. 4.3 Schematic representation of some of the optothermal techniques used in tissue studies: ΔT_s is the temperature change of a sample; ΔT_G is the temperature change of a surrounding gas; dS is the thermoelastic deformation; ϕ_d is the deflection angle of a probe laser beam; Δp is the pressure change; (1) – OA technique, (2) – OTR technique, (3) – thermal lens technique, (4) – deflection technique [29].

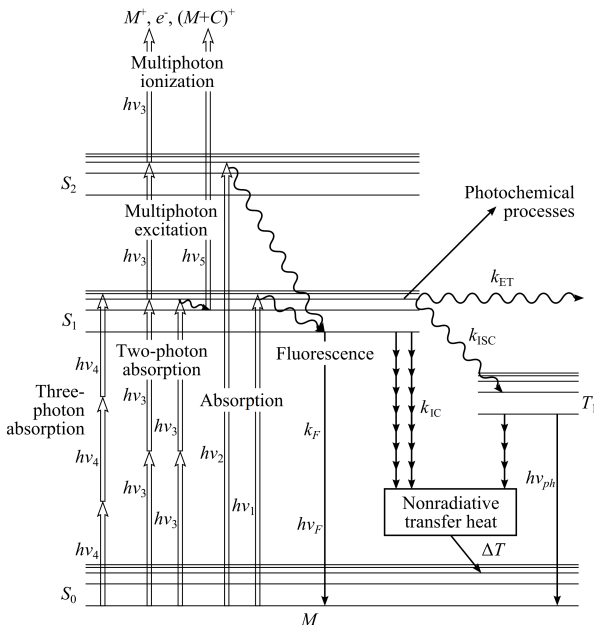


Fig. 4.4. Principles of light interaction with biomolecules basic for biomedical diagnostic methods; Jablonski diagram of molecular energy levels and transition rates: straight lines are radiative transitions and waving and multi-arrow lines are nonradiative transitions; this is schematics of excitation, ionization and relaxation processes of a molecule M of biological specimen; S_0 , S_1 and S_2 are molecule's ground and two excited singlet levels; T_1 is the molecule's excited triplet state; $h\nu_1$ and $h\nu_2$ are photon energies for excitation of S_1 and S_2 levels from the ground level S_0 , $S_0 \rightarrow S_1$ and

$S_0 \rightarrow S_2$; $h\nu_3$ is photon energy related to two-photon and multiphoton excitation and ionization; $h\nu_4$ is photon energy related to three-photon excitation; $h\nu_5$ is photon energy for ionization from the excited level S_1 ; M^+ , e^- , $(M+C)^+$ are ionization products; C is the molecule of the other type; $h\nu_F$ is the energy of fluorescing photon and k_F is the rate of fluorescence; k_{IC} is the rate of internal conversion to the ground state S_0 ; k_{ISC} is the rate of intersystem crossing from S_1 to T_1 ; k_{ET} is the rate of nonradiative energy transfer to adjacent molecules; $h\nu_{ph}$ is the energy of phosphorescing photon; ΔT is the temperature increase of the biological specimen due to nonradiative transfer; two-photon fluorescence is excited at GW/cm^2 incident intensities and multiphoton ionization requires multiple photons (e.g., 4 for NIR incident light) and TW/cm^2 intensities [3, 15].

The intensity of the signals obtained with any of the PT or PA techniques depends on the amount of energy absorbed and transformed into heat and on the thermoelastic properties of the sample and its surroundings. Assuming that nonradiative relaxation (see Fig. 4.4) is the main process in light beam decay and extinction is not very high, $\mu_a l \ll 1$ (l is the length of a cylinder within the sample occupied by a pulse laser beam), the absorbed energy can be estimated on the basis of Bouguer–Beer–Lambert law (see Eq. 3.18):

$$E_T \equiv E\mu_a l, \quad (4.6)$$

where E is the incident pulse energy, μ_a is the absorption coefficient.

Absorption of energy causes an increase in the local temperature ΔT , which is defined by the relation [15, 29, 52]

$$\Delta T = \frac{E_T}{c_p V \rho} \equiv \frac{E\mu_a l}{c_p V \rho} = \frac{E\mu_a}{\pi w_b^2 c_p \rho}, \quad (4.7)$$

where c_p is the specific heat capacity for a constant pressure, $V = \pi w_b^2 l$ is the illuminated volume, w_b is the laser beam radius, and ρ is the medium mass density. Assuming an adiabatic expansion of an illuminated volume at a constant pressure, one can calculate the change in the volume:

$$\Delta V = \pi(w_b + \Delta w_b)^2 l - \pi w_b^2 l = \beta V \Delta T \equiv \beta \frac{E\mu_a l}{c_p \rho}, \quad (4.8)$$

where Δw_b is the change in radius of a cylinder illuminated by a laser beam caused by a local temperature increase and β is the coefficient of volumetric expansion.

This expansion induces a wave propagating in a radial direction with the speed of sound. The

corresponding change of pressure Δp is proportional to the amplitude of mechanical oscillations $\Delta x_T \sim \Delta w_b$:

$$\Delta p = 2\pi f_{ac} v_{ac} \rho \Delta x_T \sim f_{ac} v_{ac} \rho \Delta w_b, \quad (4.9)$$

where f_{ac} is the frequency of acoustic oscillations and v_{ac} is the velocity of acoustic waves in a medium.

Using Eq. (4.9) and taking into account that $\Delta w_b \ll w_b$, we can finally find:

$$\Delta p \sim \frac{f_{ac}}{w_b} \cdot \frac{\beta v_{ac}}{c_p} \mu_a E. \quad (4.10)$$

Information on the absorption coefficient μ_a at a specific wavelength can be obtained from the measurements of the pressure change Δp (PA technique) (see Fig. 4.3). Equations (4.7) – (4.10) present principles of various OT and OA techniques. The information about the absorption coefficient μ_a at the definite wavelength can be received from direct measurements of the temperature change ΔT (optical calorimetry), volume change ΔV (optogeometric technique) or pressure change Δp (OA or PA technique) [15, 29, 50-58].

Using the connections between the focal length of the “thermal lens” f_T and the deflection angle of a probe laser beam φ_d with the change in a sample temperature ΔT (see Fig. 4.3), the approximate expressions describing the photorefractive methods can be written in the form:

For a “thermal lens” technique

$$\frac{1}{f_T} \approx d_p \frac{dn}{dT} \cdot \frac{\Delta T}{w_b^2}, \quad (4.11)$$

and a probe beam deflection technique as

$$\varphi_d \approx \frac{1}{n} \cdot \frac{dn}{dT} \cdot \Delta T, \quad (4.12)$$

where dn/dT is the surrounding medium or tissue refractive index temperature gradient, d_p is the length of the space where the exciting and the probe laser beams are overlapped.

An interferometer is also can be used to measure temperature change ΔT through the measurement of refractive index change. The phase shift in a measuring interferometer $\Delta\psi$ with the change in a sample temperature ΔT is expressed as

$$\Delta\psi \approx \frac{2\pi d_p}{\lambda_p} \cdot \frac{dn}{dT} \cdot \Delta T, \quad (4.13)$$

where λ_p is the wavelength of the probe beam.

The time delay (or termed relaxation time) between optical, thermal, and acoustic pulses is an important

parameter of time-resolved the PA techniques. For example, the pulse PA method can be characterized by the time delay (or acoustic relaxation time) between short optical and acoustical pulses:

$$t_{ac} \cong \frac{R}{v_{ac}}, \quad (4.14)$$

where R is the radius of target (at large probing beam diameters, $w_b > R$), and v_{ac} is the velocity of acoustic waves in a target.

The thermal relaxation time for the PT technique is defined by the time of the “thermal” wave propagation transverse to the probing laser beam with a radius [15, 29, 52]

$$\tau_T \approx \left(\frac{w_b}{2.4}\right)^2 \cdot \frac{1}{k_T}, \quad (4.15)$$

where

$$k_T = \frac{k}{\rho c_p} \quad (4.16)$$

is the thermal diffusivity of a tissue, k is the heat conductivity, and ρ is the mass density of a tissue.

For a highly scattering tissue, measurement of the stress-wave profile and amplitude should be combined with measurement of the total diffuse reflectance in order to extract separately both absorption and scattering coefficients of the sample. Absorption coefficient in a scattering tissue can be estimated from the acoustic transient profile only if the subsurface irradiance is known. For tissue irradiated with a wide laser beam (>0.1 mm), the effect of backscattering causes a higher subsurface fluence rate compared with the incident laser fluence (see Eq. 3.45). Therefore the z -axial light distribution in tissue and the corresponding stress distribution have a complex profile with a maximum at a subsurface layer. However, when the heating process is much faster than the medium expansion the stress amplitude adjacent to the irradiated surface $\delta p(0)$ and the stress exponential tail into the depth of tissue sample $\delta p(z)$ can be expressed as (see Eq. (3.45)): at surface ($z = 0$) [15, 29, 76-78]

$$\delta p(0) = \Gamma \mu_a E(0), \quad (4.17)$$

for $z > 1/\mu_{eff}$,

$$\delta p(z) = \Gamma \mu_a b_s E_0 \exp(-\mu_{eff} z). \quad (4.18)$$

Here, b_s is the factor that accounts for the effect of backscattered irradiance that increases the effective energy absorbed in the subsurface layer, μ_{eff} is defined in Eq. (3.45), $E(0)$ is the subsurface irradiance, and E_0 is

the incident laser pulse energy at the sample surface (J/cm^2). For optically thick samples

$$E(0) \approx (1 + 7.1R_d)E_0, \quad (4.19)$$

where R_d is the diffuse reflection. In Eqs. (4.17) and (4.18)

$$\Gamma = \beta \frac{v_{ac}^2}{c_T} \quad (4.20)$$

is the Grüneisen parameter, which is a dimensionless, temperature-dependent factor proportional to the fraction of thermal energy converted into mechanical stress; c_T is the specific heat of the tissue; for water, it can be expressed with an empirical formula as

$$\Gamma = 0.0043 + 0.0053 T^{\circ}C, \quad (4.21)$$

for the normal physiological temperature $T = 37^{\circ}C$, $\Gamma \approx 0.2$.

Equations (4.17) and (4.18) are strictly valid only when the heating process is much faster than expansion of the medium. The stress is temporarily confined during laser heat deposition when the duration of the laser pulse is much shorter than the time of stress propagation across the depth of light penetration in the tissue. Such conditions of temporal pressure confinement in a volume of irradiated tissue allow for the most efficient pressure generation.

The pulse laser heating of a tissue causes its temperature perturbations and corresponding modulation of the own thermal (infrared) radiation. This is the basis for the pulse photothermal radiometry (PTR) [15, 29, 54, 55, 69-71]. The maximum of intensity of thermal radiation of living objects falls at the wavelength range close to $10 \mu m$. A detailed analysis of PTR signal formation requires knowledge on the internal temperature distribution within the tissue sample, tissue thermal diffusivity, and its absorption coefficients at the excitation μ_a and emission μ_a' ($10 \mu m$) wavelengths. The knowledge of some of mentioned parameters allows one on the basis of measured PTR signal to reconstruct the spatial distribution of μ_a . For example, the surface radiometric signal $S_r(t)$ at any time t is the sum of the contributions from all depths in the tissue at time t . The radiation from deeper depths is attenuated by the infrared absorption of the sample before reaching the detector. Since the initial surface temperature is known, the temperature distribution into the sample depth can be extracted from $S_r(t)$ measurement.

PTR and PA transient techniques provide a convenient means for *in vitro* and *in vivo* monitoring of human skin properties (optical absorption, thermal properties, water content) and surface concentrations of topically applied substances (drugs and sunscreen diffusion) [15, 29, 56-78]. The use of pulsed PA and PTR techniques are more appropriate for *in vivo* and *in*

situ measurements. For example, the PT and PA flow cytometry techniques show the capability to visualize absorbing cellular structures of moving unlabeled cells in real time *in vivo* in studies of circulating red and white blood cells in capillaries, lymph microvessels and nodes of rat mesentery and mouse ear [63, 64, 68, 72-74]. The imaging of single cells *in vivo* is potentially important for the early diagnosis of diseases (e.g., cancer and diabetes) and for study of impact of various factors (e.g., drugs, nanoparticles, nicotine, and ionizing radiation) on individual cells.

4.3 Acoustooptical interactions

Acoustic wave (AW) and light interaction within a tissue as a heterogeneous medium is the basis for acoustooptical tomography (AOT) or ultrasound-modulated optical tomography, where the acoustic (ultrasound (US)) modulation of coherent laser light traveling in tissue is provided [29, 57, 80-82]. An AW is focused into tissue and laser light is irradiating the same volume within the tissue. Any light that is encoded by the ultrasound, including both singly and multiply scattered photons, contributes to the imaging signal. Axial resolution along the acoustic axis can be achieved with US-frequency sweeping and subsequent application of the Fourier transformation, whereas lateral resolution can be obtained by focusing the AW.

Three major mechanisms have been identified for the acoustic modulation of light in scattering tissues [57, 82]. The first mechanism is based on US-induced variations of the optical properties of a tissue caused by spatially and temporally dependent tissue compression or rarifying at propagation of the AW. These variations in tissue mass density cause the corresponding oscillations of tissue optical properties, including absorption and scattering coefficients, and refractive index. Accordingly, the detected intensity of light varies with the AW.

US modulation of incoherent or low-coherent light is much weaker than a highly coherent laser light.

The second mechanism is based on variations of the optical properties in response to US-induced displacement of scatterers. The displacements of scatterers, assumed to follow AW amplitudes, modulate the physical path lengths of light traveling through the acoustic field. Multiply scattered light accumulates modulated physical path lengths along its path. Consequently, the intensity of the speckles formed by the multiply scattered coherent light fluctuates with the AW.

The third mechanism is caused by US modulation of index of refraction of tissue. Oscillations of index of refraction modulate the optical path lengths of light travelling through the acoustic field. Multiply scattered light accumulates modulated optical path lengths along its complete path. Similarly to the second mechanism, the intensity of the speckles formed by the multiply scattered coherent light fluctuates with the AW.

Both the second and the third mechanisms require the use of coherent light and both may be associated

with the speckle effect. The modulation of the speckles in the second mechanism is caused by the acoustic modulation of scatterer displacements, while the modulation of the speckles in the third mechanism is caused by the acoustic modulation of refractive index of the tissue.

The intensity modulation depth M , defined as the ratio of the intensity at the fundamental frequency I_1 and the unmodulated intensity I_0 , is proportional to the squared acoustic amplitude A^2 [29, 57, 82]

$$M = \frac{I_1}{I_0} \cong \frac{1}{12} \cdot \frac{d^2}{l_{tr}^2} \varepsilon \propto A^2, \quad (4.22)$$

where

$$\begin{aligned} \varepsilon &= 6(\delta_n + \delta_d)(n_0 k_0 A)^2, \\ \delta_n &= (\alpha_{n1} + \alpha_{n2})\eta^2, \\ \delta_d &= \frac{1}{6}, \\ \alpha_{n1} &= \frac{k_a l_{tr}}{2} \arctan(k_a l_{tr}), \\ \alpha_{n2} &= \frac{\alpha_{n1}}{\frac{k_a l_{tr}}{\arctan(k_a l_{tr})} - 1}, \end{aligned} \quad (4.23)$$

d is the tissue slab thickness, n_0 is the background refractive index, k_0 is the optical wave vector in vacuum, k_a is the acoustic wave vector, and l_{tr} is the photon transport mean free path;

$$\eta = \frac{\partial n}{\partial p} \cdot \rho v_{ac}^2 \quad (4.24)$$

is the elasto-optical coefficient, related to the adiabatic piezo-optical coefficient of the tissue $\partial n / \partial p$, the mass density ρ , and the velocity of acoustic waves (speed of sound) v_{ac} . The parameters δ_n and δ_d are related to the average contributions per photon free path (or per scattering event) to the ultrasonic modulation of light intensity through index of refraction and displacement, respectively. The contribution from the index of refraction δ_n increases with $k_a l_{tr}$ because a longer photon free path, relative to the acoustic wavelength, accumulates a greater phase modulation. By contrast, the contribution from displacement δ_d stays constant at $1/6$, independent of k_a and l_{tr} . The contribution from index of refraction above a critical point at $k_a l_{tr} = 0.559$, where contributions from refractive index and displacement are equal, increases with $k_a l_{tr}$ and significantly outmatch the contribution from

displacement. The correlation between these two modulation mechanisms is neglected here for simplicity.

Equation (4.22) shows a quadratic relationship between intensity modulation depth M and the acoustic amplitude A . Only the nonlinear terms of phase accumulation contribute to the acoustic modulation of coherent light at multiple scattering. The linear term vanishes as a result of optical random walk in scattering media. In the ballistic (no scattering) regime, M is proportional to A due to none-averaged contributions from the linear term of phase accumulation. In the quasi-ballistic (minimal scattering) mode, M may show a mixed behavior with A .

5 Tissue luminescence, Raman scattering and nonlinear interactions

5.1 Definitions and one-photon fluorescence

The result of one of the fundamental mechanisms of light-tissue interaction is luminescence, which is subdivided into fluorescence, corresponding to an allowed optical transition with rather high quantum yield and short (nanosecond) lifetime, as well as phosphorescence, corresponding to a „forbidden“ transition with low quantum yield and long decay times in the microsecond – millisecond range (see Fig. 4.4) [29, 31-33, 83-97].

Absorption of light is connected with an electronic transition from a ground state to an excited state of a molecule. Light of intensity I_0 with wavelength λ passing through a layer of thickness d is thereby attenuated according to the Eqs. (3.11) and (3.14) [92]

$$I(\lambda) = I_0 \exp(-\varepsilon_\lambda c_a d), \quad (5.1)$$

where ε_λ is the molar extinction coefficient at the wavelength λ , and c_a is the concentration of absorbing molecules. In scattering samples additional reduction of transmitted light, as described in detail above, is expected.

Fluorescence arises upon light absorption and is related to an electronic transition from the excited state to the ground state of a molecule (see Fig. 4.4). Its intensity is defined as absorbed intensity multiplied by coefficient of fluorescence efficiency (or fluorescence quantum yield) η_F and by the ratio of the solid angle of detection Ω of isotropic fluorescence radiation to the total solid angle 4π

$$I_F(\lambda) = I_0 [1 - \exp(-\varepsilon_\lambda c_a d)] \eta_F \cdot \frac{\Omega}{4\pi}. \quad (5.2)$$

In the case of thin samples, e.g., cell monolayers or biopsies with a few micrometers in thickness, Eq. (5.2) can be approximated by [92]

$$I_F(\lambda) = \eta_F I_0 \epsilon_\lambda c_a d \cdot \frac{\Omega}{4\pi}. \quad (5.3)$$

This implies that fluorescence intensity is proportional to the fluorescence quantum yield of the absorbing molecules and the concentration. In scattering media, the path lengths of scattered and unscattered photons within the sample are different, and the Eqs. (5.2) and (5.3) have to be modified. However, in homogenous thin samples, the linearity between I_F , c_a and η_F is typically fulfilled.

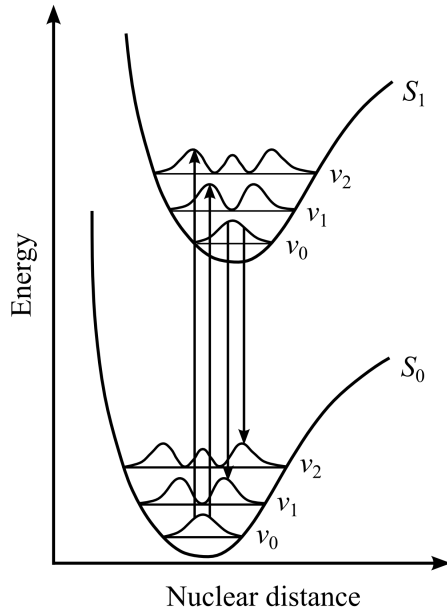


Fig. 5.1 Potential diagram of electronic states (S_0 , S_1) and vibrational levels (v_i). Vibronic wave functions and optical transitions are indicated as excitation $S_0 v_0 \rightarrow S_1 v_n$ and fluorescence $S_1 v_0 \rightarrow S_0 v_n$ [92].

Energies of the electronic states of a molecule are complex functions of the nuclear distances of relevant atoms, usually forming „potential wells“, as shown in Fig. 5.1 [92] for the ground state (S_0) and the first excited state (S_1). Each well contains a larger number of vibrational levels v_i that further split into numerous rotational levels (omitted in Figs. 4.4 and 5.1) of the molecule. Electronic transitions occur in „vertical direction“, because during their short duration nuclear coordinates do not change (Franck-Condon principle). Electronic transitions usually originate from vibronic ground states (excitation, S_0 and v_0 ; fluorescence, S_1 and v_0). The probability of each transition corresponds to the square of the transition dipole moment and is determined by an overlap of the corresponding electronic wave functions in the ground state and the excited state of the molecule. Therefore, absorption and fluorescence spectra originate from a superposition of several transitions, often resulting in broad spectral bands. From Fig. 5.1, one can deduce that the so-called 0-0 transition between the lowest vibrational levels is only slightly pronounced, since the overlap between

corresponding wave functions is very low. Therefore, fluorescence spectra are usually shifted to lower energies ΔW corresponding to higher wavelengths $\lambda = \Delta W/hc$ as compared with absorption or excitation spectra (h is the Planck’s constant, c is the velocity of light). This phenomenon is called „Stokes shift.“

If the potential curves are plotted without regard to the variable nuclear distances, the different molecular states can be illustrated in a *Jablonski diagram*, as shown in Fig. 4.4. Excitation usually occurs from the singlet ground state S_0 to various vibronic levels of the excited singlet states S_n , from where fast nonradiative transitions („internal conversion“) occur within the femtosecond time range to the lowest excited state S_1 . From S_1 , various transitions can be distinguished: fluorescence to the ground state S_0 (including its vibrational states) with a rate k_F , internal conversion to the ground state S_0 (rate k_{IC}), intersystem crossing from the singlet to the triplet state T_1 (rate k_{ISC}), and nonradiative energy transfer to adjacent molecules (rate k_{ET}). All these rates sum up according to [92]

$$k = \frac{1}{\tau} = k_F + k_{IC} + k_{ISC} + k_{ET}, \quad (5.4)$$

where τ is the lifetime of the excited state S_1 . The ratio k_F/k corresponds to the fluorescence quantum yield η_F . Although by optical spectroscopy only radiative transitions can be monitored, changes of k_{IC} or k_{ET} are often deduced from fluorescence lifetime measurements. It should be noted that the radiative transition $T_1 \rightarrow S_0$ is spin-forbidden, and only within a few specific molecules is this transition becoming prominent.

Characteristic times involved in the excitation and de-excitation of a fluorescing molecule are the following: absorption $\sim 10^{-15}$ s; vibrational relaxation $\sim 10^{-12} - 10^{-10}$ s; lifetime of the singlet excited state $S_1 \sim 10^{-10} - 10^{-7}$ s \rightarrow fluorescence; intersystem crossing $\sim 10^{-10} - 10^{-8}$ s; internal conversion $\sim 10^{-11} - 10^{-9}$ s; lifetime of the triplet excited state $T_1 > 10^{-6}$ \rightarrow phosphorescence (see Fig. 4.4).

Transition dipole moments have defined orientations within a molecule. Upon excitation with linear polarized light, one preferentially excites those molecules, whose transition dipoles are parallel to the electric field vector of incident light. This selective excitation of an oriented population of molecules results in partially polarized fluorescence, which is described by the degree of polarization (see Eq. (3.96)) [83, 83-97]:

$$P_L^F = \frac{I_{\parallel}^F - I_{\perp}^F}{I_{\parallel}^F + I_{\perp}^F} \quad (5.5)$$

or by fluorescence anisotropy

$$r_F = \frac{I_{\parallel}^F - I_{\perp}^F}{I_{\parallel}^F + 2I_{\perp}^F} \quad (5.6)$$

with I_{\parallel}^F and I_{\perp}^F being the fluorescence intensities of light polarized parallel or perpendicular to the exciting electric field vector, respectively. Usually, P_L^F and r_F depend on the time interval between excitation and fluorescence detection, since during the lifetime of their excited states, many molecules change their orientation by rotation („rotational diffusion“). From time-resolved measurements of fluorescence anisotropy, a time constant τ_r of rotational diffusion can be determined that is correlated with the volume V_M of the molecule and the viscosity η_{env} of its environment according to [92]

$$\tau_r = \frac{\eta_{env} V_M}{k_B T}, \quad (5.7)$$

where k_B is the Boltzmann constant and T is the absolute temperature (see Eq. (3.78)). Time constants of rotational diffusion of about 13 ns is correlated with a molecular weight of proteins around 50 kilodaltons, whereas a time constant around 300 ps is attributed to an aggregated species of a protoporphyrin with a 1.6 nm diameter.

At excitation biological tissue by ultraviolet light ($\lambda \leq 370$ nm), fluorescence of proteins as well as of nucleic acids can be observed [92]. Fluorescence quantum yields of all nucleic acid constituents, however, are around 10^{-4} – 10^{-5} , corresponding to lifetimes of the excited states in the picosecond time range. Autofluorescence of proteins is related to the amino acids phenylalanine, tyrosin and tryptophan with absorption maxima at 257 nm, 275 nm and 280 nm, respectively, and emission maxima between 280 nm (phenylalanine) and 350 nm (tryptophan). Usually the protein spectrum is dominated by tryptophan. Fluorescence from collagen or elastin is excited between 300 and 400 nm and shows broad emission bands between 400 and 600 nm with maxima around 400 nm, 430 nm and 460 nm. In particular, fluorescence of collagen and elastin can be used to distinguish various types of tissues, e.g. epithelial and connective tissue.

The reduced form of coenzyme nicotinamide adenine dinucleotide (NADH) is excited selectively in a wavelength range between 330 and 370 nm [92]. NADH is most concentrated within mitochondria where it is oxidized within the respiratory chain located within the inner mitochondrial membrane and its fluorescence is an appropriate parameter for detection of ischemic or neoplastic tissues. Fluorescence of free and protein-bound NADH has been shown to be sensitive on oxygen concentration. Flavin mononucleotide (FMN) and dinucleotide (FAD) with excitation maxima around 380 nm and 450 nm have also been reported to contribute to intrinsic cellular fluorescence.

Porphyrin molecules, e.g. protoporphyrin, coproporphyrin, uroporphyrin or hematoporphyrin occur within the pathway of biosynthesis of hemoglobin, myoglobin and cytochromes, thus intrinsic fluorescence of these molecules provides information related to disease development. For example, abnormalities in heme synthesis, occurring in the cases of porphyrias and some hemolytic diseases, may enhance considerably the porphyrin level within tissues, which could be detected via tissue autofluorescence associated with porphyrin bands. Several bacteria, e.g. *Propionibacterium acnes* or bacteria within dental plaque (biofilm), such as *Porphyromonas gingivalis*, *Prevotella intermedia*, and *Prevotella nigrescens*, accumulate considerable amounts of protoporphyrin. Therefore, acne or caries detection based on measurements of intrinsic fluorescence appears to be a promising method.

At present various exogenous fluorescing dyes can be applied for probing of cell anatomy and cell physiology. In humans such dyes as fluorescein and indocyanine green are on use for fluorescence angiography or blood volume determination [31, 87, 88]. Novel fluorescent contrast agents for optical imaging of *in vivo* tumors based on a receptor-targeted dye-peptide conjugate and green fluorescent protein platforms are available.

Fluorescence spectra often give detailed information on fluorescent molecules, their conformation, binding sites and interaction within cells and tissues. Fluorescence intensity can be measured either as a function of the emission wavelength or of the excitation wavelength. The fluorescence emission spectrum $I_F(\lambda)$ is specific for any fluorophore and commonly used in fluorescence diagnostics.

Various comprehensive and powerful fluorescence spectroscopies such as microspectrofluorimetry, polarization anisotropy, time-resolved with pulse excitation and frequency domain, time-gated, total internal reflection fluorescence spectroscopy and microscopy, fluorescence resonant energy transfer method, confocal laser scanning microscopy, and their combinations are available now. Principles of optical clinical chemistry based on measuring of changes of fluorescence intensity, wavelength, polarization anisotropy, and lifetime are described in literature [29, 31-33, 83-97]. Various fluorescence techniques of selective oxygen sensing and blood glucose and blood gases detection are available.

For example, human skin contains various types of native fluorophores with unique absorption and emission spectra, different fluorescence quantum efficiency, different fluorescence decay time, and different distribution within the skin [91]. However some fluorophores have similar absorption and fluorescence spectra, and thus, fluorescence spectra measured on the skin surface are the result of the overlapping bands of such fluorophores. The skin also contains low-fluorescing chromophores, such as hemoglobin and melanin, which due to their high

concentration may absorb fluorescence light emitted by the other fluorophores, thus may modify initial fluorescence spectra due to filtering properties of the chromophores.

When the excitation wavelength is increased new fluorophores are involved in the formation of the shape of fluorescence spectrum. The closer the excitation wavelength to the therapeutic/diagnostic window (600–900 nm), the larger the penetration depth of the excitation light in tissue and the larger tissue volume is probed by the excitation light. As a result, other fluorophores located in deeper skin layers contribute to the total tissue fluorescence intensity [91].

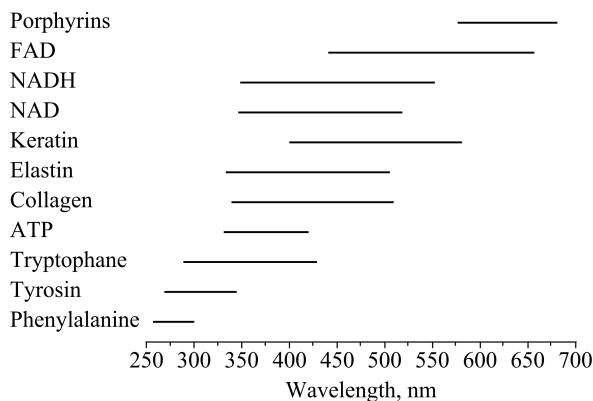


Fig. 5.2. Spectral ranges of fluorescence of the main skin and other tissue fluorophores [91].

The spectral ranges of fluorescence of the main skin fluorophores are presented in Fig. 5.2. It can be seen that the skin autofluorescence in the UVA range is dominated by the fluorescence bands of aromatic amino acids, namely tyrosine and tryptophan. Tyrosine and tryptophan content in epidermis is more than twice that of the whole skin, and this is why epidermis has high autofluorescence in the UVA range. This also explains why the fluorescence of psoriatic stratum corneum is significantly higher than that for normal stratum corneum.

Among the endogenous skin fluorophores are the different forms of NAD and keratin located in the epidermis and collagen in the dermis. The reduced (NADH) and oxidized (NAD⁺) forms of NAD take part in cellular metabolism, and the intensity of their specific fluorescence (fluorescence maxima near 460 nm and 435 nm respectively) is used for the quantitative NADH detection and differential diagnostics of the metabolism dysfunction. A similarity between the autofluorescence spectrum of the human skin *in vivo* with maximum near 450 nm and the emission spectrum of the keratin which molecules are composed from a number of amino acids was found.

Collagen is one of the most important skin fluorophores. Approximately 75% of the dry weight of the dermal tissue is composed of the collagen fibres. Collagen is the main structural component of the connective tissue and accounts for about 90% of protein in human dermis. There are at least five types of

collagen; types I (about 80%) and III (about 20%) are found in dermal collagen, and type IV is found in the cellular basement membrane. Collagen fibres exhibit a constant density throughout all dermal layers.

5.2 Multiphoton fluorescence

Novel laser spectroscopic techniques for tissues and cells studies are associated with nonlinear spectroscopies, in particular multiphoton (two-photon and three-photon) scanning fluorescence microscopy and optical harmonic generation (second-harmonic generation (SHG) and triple-harmonic generation (THG)) microscopy, which makes it possible to provide *in vivo* functional imaging [16, 19-23, 26, 27, 29, 98-103]. The two-photon technique employs both ballistic and scattered photons at the wavelength of the second harmonic of incident radiation coming to a wide-aperture photodetector exactly from the focal area of the excitation beam. A unique advantage of two-photon microscopy is the possibility of investigating three-dimensional distributions of chromophores excited with ultraviolet radiation in thick samples. This becomes possible because chromophores can be excited (e.g., at the wavelength of 350 nm) with laser radiation whose wavelength (e.g., 700 nm) falls within the range where a tissue has a high transparency (low absorption). The excitation radiation reaches deeper layers and produces less damage in tissues. Fluorescent emission in this case lies in the visible range (>400 nm) and comparatively easily emerges from a tissue and reaches a photodetector, which registers only the legitimate signal from the focal volume without any extraneous background.

Multiphoton absorption requires high light intensities in the range 100 MW/cm² up to TW/cm². Most multiphoton microscopes are based on femtosecond laser pulses at MHz repetition rate with high kilowatt peak power (P) and low mean power in the μ W/mW range. Figure 4.4 demonstrates the principles of multiphoton excitation and ionization, especially two-photon excitation where two NIR photons are absorbed simultaneously to induce a single visible fluorescence photon. The multiphoton efficiency of an n -photon process follows a P^n relation. In the case of two-photon microscopy, the two-photon effect depends on P^2/τ_p . The shorter the pulse width (τ_p) and the higher the laser power the more fluorescence photons.

The instant intensity of two-photon-excited fluorescence (TPEF) is a function of the average incident power (P_0), the pulse width (τ_p), the pulse repetition rate (f_p), the two-photon absorption cross section [$\sigma_2 = \sigma_2(\lambda_{exc})$], fluorescence quantum yield [$\eta = \eta(\lambda_{em})$], and the numerical aperture (NA) of the microscope objective that focuses the light [29, 99]:

$$I_{2f}(t) = \kappa \left(\frac{4}{\pi} \right)^2 \sigma_2 \eta \left(\frac{P_0}{\tau_p f_p} \right)^2 \left[\frac{(NA)^2}{hc \lambda_{exc}} \right]^2, \quad (5.8)$$

where κ is the coefficient accounting for the collection efficiency of the fluorescent photons, h is Planck's constant, c is the speed of light, and λ_{exc} is the excitation wavelength. The derivation of this equation assumes negligible saturation of the fluorophore and that the paraxial approximation is valid.

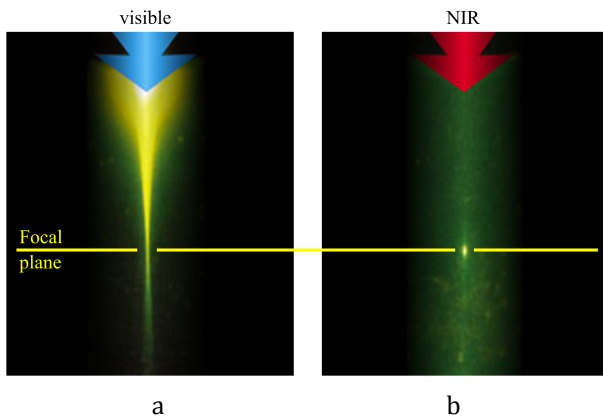


Fig. 5.3 The comparison of one-photon (a) and two-photon (b) fluorescence excitation in tissues [100].

Nonlinear microscopies are based on the application of low energy photons in the NIR between 700 and 1200 nm within the “optical window” where the one-photon absorption coefficients and scattering coefficients of unstained cells and tissues are low. Most cells (except erythrocytes and melanocytes) appear transparent in this wavelength range. A significant advantage of multiphoton microscopy compared to conventional one-photon microscopy is the tiny sub-femtoliter excitation volume (see Fig. 5.3). Absorption in out-of-focus regions is avoided because the probability of two-photon absorption decreases nearly with the distance d from the focal point according to a d^{-4} relation. In comparison to one-photon fluorescence microscopy, including confocal microscopy, with large excitation cones (see Fig. 5.3a) and the subsequent problem of out-of-focus damage as well as the disadvantage of using high-energy excitation photons, the two-photon and other multiphoton microscopies are more precise and less invasive at tissue optical sectioning. The femtosecond NIR laser radiation exposure of living cells for hours with a high 200 GW/cm² peak intensity did not show any impact on cellular reproduction and vitality.

Investigations of tissues and cells by means of two-photon microscopy are characterized by the following typical parameters of laser systems: the wavelength ranges from 700 to 960 nm, the pulse duration is on the order of 150 fs, the pulse repetition rate is 76–80 MHz, and the mean power is less than 10 mW [16, 19-23, 26, 27, 29, 98-103]. Such parameters can be achieved with mode-locked dye lasers pumped by Nd: YAG laser, titanium sapphire lasers pumped by an argon laser, diode-pumped solid-state lasers, and fiber lasers. Thanks to the small excitation volume (Fig. 5.3a), multiphoton microscopy does not require confocal units or de-scanned detection systems.

In addition to conventional one-photon microscopes, multiphoton microscopy enables SHG and THG imaging (see section 5.4).

5.3 Sonoluminescence

A sonoluminescence (SL) signal is generated internally in the media with a MHz-range continuous-wave ultrasound (US) [29, 104]. The light emission phenomenon is connected with driving of small bubbles by US collapse. The bubbles start out with a radius of several microns and expand to approximately $\sim 50 \mu\text{m}$, owing to a decrease in acoustic pressure in the negative half of a sinusoidal period; after the acoustic wave reaches the positive half of the period, the resulting pressure difference leads to a rapid collapse of the bubbles, accompanied by a broadband emission of light – SL. Such emission is of a short duration (in tens of picoseconds), repeatable with each cycle of sound, and has the spectrum containing molecular emission bands (with peaks near 300-500 nm) associated with the liquid, mostly water, in which the SL occurs.

It was shown experimentally that there is a threshold of SL generation at applied US pressure, when the peak US pressure at the US focus was ~ 2 bars. The rapid increase of the SL intensity with the acoustic pressure above the threshold indicates that the SL signal would be a sensitive measure of the local acoustic pressure.

As a new approach for optical imaging of biological tissues, the major advantages of SL include: (1) high signal-to-noise ratio due to the internally generated probe optical signal; (2) high contrast of imaging; (3) good spatial resolution, which is limited by the US focal size; and (4) low cost of equipment.

SL-based tomography is based on several contrast mechanisms [104]: (1) for the objects with US contrast relative to the background, the SL signal originating from the object will differ from that originating from the background medium, the SL generation is affected by the local US intensity; (2) for the objects with contrast in optical properties, the SL signal from the object is attenuated differently because the SL light must propagate through the object; (3) for objects with the ability to generate SL, the SL from the object is different, even if the local US pressure is the same.

It should be noted that the peak pressure at the US focus is typically less than ~ 2 bars (1.3 W/cm² in spatial-peak-temporal-peak power), which is one order in magnitude less than the safety limit set by the U.S. FDA (23 bars) and two orders less than the tissue damage threshold (400 and 900 W/cm² at 1 MHz for brain and muscle, respectively).

5.4 Second harmonic generation

At intensive light interaction with noncentrosymmetrical tissue structures such as collagen, two photons interact simultaneously and generate coherent radiation at exactly half of the excitation wavelength in the forward direction – this is the origin of the second harmonic generation (SHG) [16, 19-23,

29, 26, 27, 99, 101-103, 105]. There is no light absorption, thus, both photobleaching and photodamage associated with SHG are excluded. The technique enables deep 3D imaging due to backscattering of light on the second harmonic.

SHG is a second order nonlinear optical process that can only arise from media lacking a centre of symmetry, e.g., an anisotropic crystal or at an interface such as membrane. It can be used to image highly ordered structural proteins without any exogenous labelling, as well as biological membranes with high membrane specificity.

Collagen as a main component of connective tissues has an appreciable nonlinear susceptibility for SHG. The helix of collagen secondary structure is noncentrosymmetric, satisfying a condition for SHG, which self-assembles into higher order structures. Collagen has been shown to have a dominant uniaxial second-order nonlinear susceptibility component aligned along the fibre axis. In such multi-component tissues as skin, SHG light is generated mostly within dermis, not in cellular layers like epidermis or subcutaneous fat. SHG techniques has a number advantages connected with the incident wavelength dividing and selectivity to tissue structure, which allow one to reject easily surface reflection and multiple scattering of the incident light in the epidermis layer without any gating technique. In addition, SHG polarimetry is an effective tool to probe collagen orientation in the tissues.

In general, the nonlinear polarization for a material can be expressed as [27, 29, 105]

$$P_{material} = \chi^{(1)}\vec{E} + \chi^{(2)}\vec{E}\vec{E} + \chi^{(3)}\vec{E}\vec{E}\vec{E} + \dots, \quad (5.9)$$

where $P_{material}$ is the induced polarization, $\chi^{(n)}$ is the n th order nonlinear susceptibility, and \vec{E} is the electric field vector of the incident light. The first term describes normal absorption and reflection of light; the second, SHG, sum, and difference frequency generation; and the third, both two- and three-photon absorption, as well as third harmonic generation.

SHG, by contrast to two-photon fluorescence (see section 5.2), does not arise from an absorptive process. Instead, the intense laser field induces a nonlinear, second order, polarization in the assembly of molecules, resulting in the production of a coherent wave at exactly twice the incident frequency (or half the wavelength). The spectral and temporal profiles of two-photon excited fluorescence and SHG are also different. For two-photon fluorescence, the width of the emission spectrum is determined by the relative geometries of the ground and excited molecular state (see Fig. 4.4) and the emission lifetime is related to the oscillator strength of the transition and is typically on the order of a few nanoseconds. In SHG, by contrast, both the spectral and temporal characteristics are derived from the laser source: the bandwidth scales as $1/\sqrt{2}$ of the bandwidth of excitation laser, and, due to the coherence of the

process, the SHG pulse is temporally synchronous with the excitation pulse.

A simplified expression for the SHG signal intensity has a form [27, 29, 105]

$$I(2\omega) \propto \left[\chi^{(2)} \frac{E(\omega)}{\tau_p} \right]^2 \tau_p, \quad (5.10)$$

where $\chi^{(2)}$ is the second order nonlinear susceptibility, $E(\omega)$ and τ_p are the laser pulse energy and width, respectively. As in two-photon fluorescence (see Eq. (5.8)), the signal is quadratic with peak power, but since SHG is an instantaneous process, a signal is generated during only the duration of the laser pulse. The macroscopic value $\chi^{(2)}$ can be expressed in terms of the first molecular hyperpolarizability β_M as

$$\chi^{(2)} = \rho_M \langle \beta_M \rangle, \quad (5.11)$$

where ρ_M is the density of molecules and the brackets denote an orientation average. It follows from Eqs. (5.10) and (5.11) that SHG signal depends on the square of the density of molecules whereas two-photon fluorescence intensity is linear with the absorption cross section of fluorophores (see Eq. (5.8)).

Within the two-level system model, the first molecular hyperpolarizability β_M is given by [27, 29, 105]

$$\beta_M = \frac{3e^2}{2\hbar^3} \frac{\omega_{ge} f_{ge} \Delta\mu_{ge}}{[\omega_{ge}^2 - \omega^2][\omega_{ge}^2 - 4\omega^2]}, \quad (5.12)$$

where e is the electron charge, $\hbar \equiv h/2\pi$ is the reduced Planck constant, $\hbar\omega_{ge}$, f_{ge} , and $\Delta\mu_{ge}$ are the energy difference, oscillator strength, and change in dipole moment between the ground and excited states, respectively. While SHG is not an absorptive process, the magnitude of the SHG wave can be resonance enhanced when the energy of the second harmonic signal overlaps with an electronic absorption band. It follows from Eq. (5.12) that β_M becomes large when the laser fundamental frequency approaches the electronic transition then the total second order response is a sum of the nonresonant and resonant contributions:

$$\chi_{total}^{(2)} = \chi_{nonres}^{(2)} + \chi_{res}^{(2)}. \quad (5.13)$$

Depending upon the specific properties of the molecule and the excitation wavelength, the resonant contribution can dominate, resulting in enhancement of an order of magnitude or more.

5.5 Vibrational energy states excitation and Raman scattering

Mid infrared (MIR) and Raman spectroscopies use light excited vibrational energy states in molecules to get information about the molecular composition, molecular structures and molecular interactions in a sample [20-24, 26, 34, 106-117]. In MIR-spectroscopy infrared light from a broadband source (usual wavelength range $\lambda = 2.5\text{--}25\ \mu\text{m}$ or wavenumber range $\tilde{\nu} = 1/\lambda = 4000\text{--}400\ \text{cm}^{-1}$) is directly absorbed to excite the molecules to higher vibrational states v'' (Fig. 5.4).

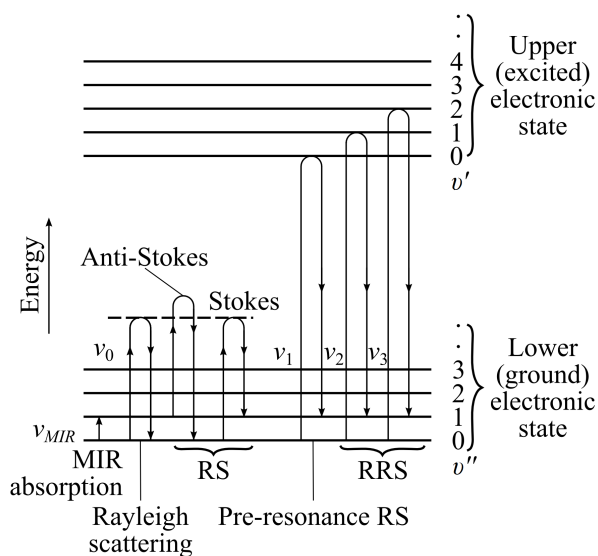


Fig. 5.4 Illustration of MIR absorption, Rayleigh and Raman scattering using a molecular energy level diagram; v'' and v' are vibrational states; RS – Raman scattering, RRS – Resonance Raman scattering.

In a Raman scattering event, light is inelastically scattered by a molecule, when a small amount of energy is transferred from the photon to the molecule (or vice versa) (Fig. 5.4). This leads to an excitation of the molecule from usually its lowest vibrational energy level in the electronic ground state to a higher vibrational state. At Raman scattering there is the change of wavelength of the scattered light. The collection of new wavelengths (frequencies) is characteristic to the molecular structure of the scattering medium and differs from the fluorescence spectrum in being much less intense and unrelated to an absorption band of the medium. The frequencies of new lines are combinations of the frequency of the incident light and the frequencies of the molecular vibrational and rotational transitions.

There are a variety of Raman effects such as resonance Raman scattering (RRS), surface-enhanced Raman scattering (SERS), stimulated Raman scattering (SRS), and coherent anti-Stokes Raman scattering (CARS), which can considerably improve typically low signal intensities of spontaneous Raman scattering and/or provide lesser fluorescence background from most biomolecules.

The energy (frequency) difference between incident ($h\nu_0$) and Raman scattered photon ($h\nu$) is expressed as a wavenumber shift [114],

$$\Delta\tilde{k} = (\tilde{\nu}_0 - \tilde{\nu}) = \frac{1}{\lambda_0} - \frac{1}{\lambda}. \quad (5.14)$$

When the energy of the Raman scattered photons is lower than the energy of the incident photons, the process is called Stokes-Raman scattering. When a photon interacts with a molecule in a higher vibrational level, anti-Stokes Raman scattering can occur, in which the energy of the Raman scattered photons is higher than the energy of the incident photons (see Fig. 5.4). The intensity ratio of the anti-Stokes (I_{AS}) and Stokes (I_S) Raman lines for a given vibrational state is given by [114]

$$\frac{I_{AS}}{I_S} = \frac{(v_0 + v_{vib})^4}{(v_0 - v_{vib})^4} \cdot \exp\left(-\frac{hv_{vib}}{k_B T}\right), \quad (5.15)$$

where $\Delta E_{vib} = hv_{vib}$ is the energy of the molecular vibrational state. It follows that at room temperature the intensity of Stokes-Raman lines in the most informative spectral region ($> 400\ \text{cm}^{-1}$) is much higher than that of the anti-Stokes-Raman lines. In its turn, the intensity of Stokes-Raman scattered light is very low, typically 10^{-7} to 10^{-15} times the intensity of the excitation light and Rayleigh scattering. The real-time detection of Raman scattering spectra became practical because of the commercial development of lasers and subsequent advances in detector technology.

Some vibrations can be excited by both Raman and MIR processes, others can only be excited by either a Raman scattering or by MIR-absorption. Both techniques enable recording of high quality spectra in relative short acquisition times (30–60s).

The MIR and Raman spectroscopy techniques are successfully applied in various areas of clinical studies, such as cancerous tissues examination, the mineralization process of bone and teeth tissues monitoring, glucose sensing in blood, noninvasive diagnosis of skin lesions on benign or malignant cells, monitoring of treatments and topically applied substances (e.g. drugs, cosmetics, moisturizers, etc) in skin and water exchange in human eye lens [20-24, 26, 29, 34, 106-117].

Raman spectroscopy is widely used in biological studies, ranging from studies of purified biological compounds to investigations at the level of single cells. At present combinations of spectroscopic techniques such as MIR and Raman with microscopic imaging techniques are explored to map molecular distributions at specific vibrational frequencies on samples to locally characterize tissues or cells. Chemical imaging will become more and more important in the clinical diagnosis [21].

Resonance Raman scattering (RRS) is a Raman scattering technique which allows one to enhance spontaneous Raman signal and, thus, to overcome the major disadvantage of low signal intensities from most biomolecules (see Fig. 5.4) [22, 114]. It probes vibrations of chromophores and requires careful selection of the excitation wavelength to be within the absorption band of a chromophore. The generally weaker Raman signals can be detected in the presence of intense overlapping fluorescence if the Stokes shift of the fluorescence emission is large or if the faster scattering process is registered before the fluorescence emission using time-gating techniques.

Surface-enhanced Raman scattering (SERS) allows for a strong increase in Raman signals from molecules if those molecules are attached to submicron metallic structures [20-22, 113]. For a rough surface, due to excitation of electromagnetic resonances by the incident radiation, such enhancement may be of a few orders. Both the excitation and Raman scattered fields contribute to this enhancement, thus, the SERS signal is proportional to the fourth power of the field enhancement factor.

Stimulated Raman scattering (SRS) is a phenomenon, when a lower frequency 'signal' photon induces the inelastic scattering of a higher-frequency 'pump' photon in a nonlinear optical medium. As a result of this process, another 'signal' photon is produced, with the surplus energy resonantly passed to the vibrational states of the nonlinear medium. This process is the basic for Raman amplifier.

Coherent anti-Stokes Raman scattering (CARS) is a nonlinear variant of Raman spectroscopy which combines beside signal enhancement by more than four orders of magnitude further advantages such as directional emission, narrow spectral bandwidth and no disturbing interference with autofluorescence because the CARS signal is detected on the short wavelength side of the excitation radiation [21, 117]. CARS signal is usually weaker than Stokes Raman scattering because an excited vibrational state has to be populated before the scattering process. The excitation scheme of CARS involving a pump laser, a Stokes laser and probe laser enables to generate a strongly amplified anti-Stokes signal. The macroscopic polarization $P_{material}$ which is induced by an electric field E is expressed by Eq. (5.9), where $\chi^{(n)}$ is the susceptibility tensor of rank n which is a property of material. For most of bulk samples $\chi^{(2)}$ is close to zero due to symmetry requirement and $\chi^{(3)}$ becomes the dominant nonlinear susceptibility contribution. As CARS depends on $\chi^{(3)}$ and $\chi^{(1)} \gg \chi^{(3)}$, the nonlinear effect can only be detected using extraordinary intense electric fields in the megawatt (MW) range that are produced by nanosecond to femtosecond laser pulses.

5.6 Terahertz radiation interactions

The terahertz frequency range lying between the IR and microwave ranges can be expressed in different terms accounting for that $1 \text{ THz} \rightarrow 1 \text{ ps} \rightarrow 300 \text{ } \mu\text{m} \rightarrow 33 \text{ cm}^{-1} \rightarrow 4.1 \text{ meV} \rightarrow 47.6 \text{ K}$ (see Fig. 1.3). Terahertz radiation is perspective for molecular spectroscopy and biomedical applications [15, 29, 118-124]. It is known that tissues have small dispersion and large absorption in the terahertz range. Many vibrational transitions in simple biomolecules are located in this range. Terahertz absorption spectra are very sensitive to intramolecular interactions and molecules conformation change. In addition, inhomogeneities smaller than 0.1 mm producing strong scattering in the visible and NIR do not cause scattering for the terahertz. The nonionizing examination of tissues in the terahertz frequency range may have some additional advantages to very powerful NIR methods in detection and visualization of metabolic and pathological processes in tissues.

A several methods can be used for the generation of terahertz pulses, in which short laser pulses are converted to the terahertz range in photoconductive dipole antennas, semiconductor surfaces or nonlinear crystals. In the first two cases, radiation is generated due to the excitation of the transient electron-hole photoconduction in a semiconductor irradiated by light pulses and photocurrent splash caused by the action of the external or internal electric field. For the nonlinear crystal, signal is generated on the difference frequency lying in the THz-range (so called optical rectification) [118-124]. Terahertz pulses (THPs) are detected by a similar photoconductive antenna or with the help of the electrooptical effect in a nonlinear crystal. One of the main advantages of the THz time-domain spectroscopy (THz-TDS) is to provide on the basis of Fourier transform of the temporal THP profile a straightforward measurement of electromagnetic field amplitude and phase, which allows for the direct calculation of the refractive index, absorption coefficient and dispersion of the medium under study. In addition, THz-TDS has a good signal-to-noise ratio (SNR), picosecond time resolution, and a wide spectral range. Typically, SNR is more than 10^3 in the spectral range from 0.3 to 2.5 THz with a spectral resolution of 10 GHz, with pulse repetition rate of 12 ns, and the THP energy for probing a biological tissue being $\sim 10^{-13}$ J. Such low pulse energy should not damage any tissue or cell.

To calculate optical properties of a tissue it is necessary to reconstruct optical parameters from the transmission or reflectance spectra. For example, the field transmission spectrum $T_A(\omega)$ is follow up from Fourier transform of the measured pulse profiles for the amplitudes of the incident $E_i(\omega)$ and transmitted $E_T(\omega)$ fields as [118, 123]:

$$T_A(\omega) = \frac{E_T}{E_i} = T_{A0}(\omega) \cdot FP(\omega) \cdot RL(\omega), \quad (5.16)$$

where

$$T_{A0}(\omega) = \exp\left[-i\left(n_{tissue}(\omega) - n_{surround}(\omega)\right)\right] \cdot \frac{d\omega}{c} \quad (5.17)$$

contains the basic information on the tissue through which THP passing (the absorption coefficient and refractive index of the specimen); $n_{tissue}(\omega)$ and $n_{surround}(\omega)$ are the complex indices of refraction of tissue and surrounding medium, respectively;

$$FP(\omega) = \left[1 - R_A^2(\omega) \exp\left(-i2n_{tissue}(\omega) \cdot \frac{d\omega}{c}\right)\right]^{-1} \quad (5.18)$$

describes multiply reflected pulses in a parallel plate, so called Fabry–Perot modes;

$$RL(\omega) = \frac{4n_{tissue}(\omega)n_{surround}(\omega)}{\left(n_{tissue}(\omega) + n_{surround}(\omega)\right)^2} = 1 - R_A^2(\omega) \quad (5.19)$$

describes reflection losses on tissue specimen boundaries;

$$n_i(\omega) = n'_i(\omega) + i \cdot n''_i(\omega) \quad (5.20)$$

are the complex refractive indices for the corresponding medium, $i = tissue$ or $surround$;

$$n''_i(\omega) = \alpha(\omega) \cdot \frac{c}{\omega}, \quad (5.21)$$

$\alpha(\omega)$ is the absorption coefficient for radiation field which is twice less than for radiation power; $\omega = 2\pi f$ is the cyclical frequency of the THz field;

$$R_A(\omega) = \frac{n_{tissue}(\omega) - n_{surround}(\omega)}{n_{tissue}(\omega) + n_{surround}(\omega)} \quad (5.22)$$

is the complex amplitude (A) reflection coefficient; c is the speed of light.

By assuming that $RL(\omega) \approx \text{const}$, and $FP(\omega) \approx 1$, the field absorption coefficient $\alpha(\omega)$ can be obtained as:

$$\alpha(\omega) \cdot d \cong -\left\{\ln|T_A(\omega)| + \ln\left[1 - R_{av}^2\right]\right\}, \quad (5.23)$$

where $n_{surround} = 1$, and d is the thickness of specimen.

$$R_{av} \cong \frac{n_{av} - 1}{n_{av} + 1} \quad (5.24)$$

is the reflection coefficient, for the real part of the refractive index of the tissue specimen, averaged over the frequency range of the measurements. The averaged refractive index n_{av} can be determined from the time

delay Δt of a pulse propagating through the specimen [118, 123]

$$n_{av} = 1 + \Delta t \cdot \frac{c}{d}, \quad (5.25)$$

and the frequency dependence of the refractive index is determined by:

$$n'_{tissue}(\omega) = 1 + \arg\left[T_A(\omega)\right] \cdot \frac{c}{\omega \cdot d}. \quad (5.26)$$

In some specific cases, it is necessary to take into account multiple reflections from the specimen edges – Fabry–Perot modes; this is especially important in the case of large refractive indices and thin specimens, such as tooth slices or pressed medicine pellets [121].

Transmission spectroscopy is not suitable to investigate majority of tissues and living organs because of their large absorption due to high concentration of water and large sizes, especially at *in vivo* measurements. Therefore, reflection spectroscopy could be more attractive. The expression for the complex amplitude reflection coefficient, which follows from Fresnel formula for the field (see Fresnel formulas for intensities, Eqs. (3.1)–(3.4)) and accounting for the complex part of the refractive index (see Eqs. (5.20) and (5.21)), has a view [118, 123]

$$\tilde{R}_p(\omega) = \frac{n^2(\omega)\cos(\varphi) - \sqrt{n^2(\omega) - \sin^2(\varphi)}}{n^2(\omega)\cos(\varphi) + \sqrt{n^2(\omega) - \sin^2(\varphi)}}, \quad (5.27)$$

where the subscript p denotes polarization of radiation in the plane of incidence, φ is the incident angle. It can be presented as $\tilde{R}_p = R_{Ap} e^{i\phi_p}$ with amplitude R_{Ap} and phase ϕ_p . The p -polarization is highly sensitive to absorption bands of materials under study if the angle of incidence is selected nearby the angle: $\varphi_{Brewster} = \arctan n'$ (see Eq. (3.9)). For the layered tissues with layer thickness equal or greater than 100 μm , terahertz pulses reflected from different interfaces can be separated in time. By applying of expression (5.27) for each layer with its own reflection coefficient and expression (5.16) for transmittance with bulk parameters of the layer between interfaces through which radiation passes twice, propagation of terahertz radiation through a complex stratified tissue can be described [121]. The negligible inclusion of scattering for terahertz wave transportation in tissues makes this simple approach sufficiently precise.

Sometimes to study soft tissues or aqueous solutions, the attenuated total internal reflection (ATR) spectroscopy is more acceptable. Tissue or solution is probed within the penetration depth δ of the radiation field into specimen along axis z [118, 123]

$$E(z) = E_0 \exp\left(-\frac{z}{\delta}\right), \quad (5.28)$$

$$\delta \approx \frac{\lambda}{\pi} \sqrt{n_{prism}^2 \sin^2 \varphi - n_{tissue}^2}, \quad (5.29)$$

where n_{prism} is the index of refraction ATR prism material; the critical incident angle φ is defined by relation (3.10). Typically, a silicon Doe prism with the apex angle of 90° is used. The refractive index of silicon in the terahertz range is 3.42, while dispersion and absorption are practically zero. This prism placed in a collimated terahertz beam does not change its direction (see Fig. 5.5). As the reference signal, reflection by the clean working surface of the prism is used. At tissue measurement, a specimen is attached to the working surface, where evanescent field is formed, or *in vivo* tissue is pressed against the prism base (working surface). For liquids under study, a drop of material on the working surface of the prism is enough. Fresnel formulas describing the reflection spectrum are also valid for ATR if the refractive index of the prism is taken into account and n is replaced by n_{prism} in Eq. (5.27).

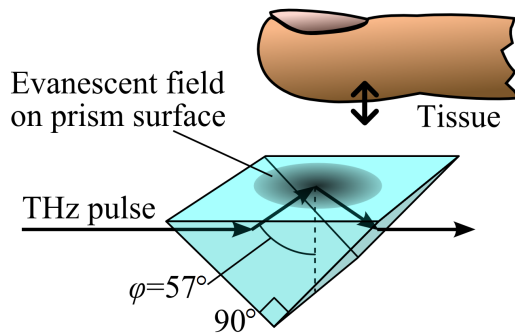


Fig. 5.5 The silicon Doe prism with the apex angle of 90° for ATR terahertz spectroscopy of tissues and liquids [118, 123].

The results of ATR experiments with water and the human skin (*in vivo*) are shown in Fig. 5.6 [118, 123]. The most important substance contained in living systems is liquid water, its average content in biological tissues achieving 75%. Liquid water strongly absorbs radiation in the terahertz range. A 200- μm -thick water layer attenuates the radiation intensity at THz frequency by an order of magnitude, while a 1-mm-thick water layer is almost opaque in the whole terahertz range. The dielectric response of liquid water is governed by several physical processes. Major contributions are attributed to two processes of relaxation dynamics characterized by slow (~ 10 ps) and fast ($\sim 200\text{--}300$ fs) relaxation times. The slow relaxation rate may be associated with dielectric relaxation processes, as the fast relaxation process is generally assigned to the intermolecular and intramolecular vibrational modes. The intermolecular stretch mode is resonant at 0.89 THz

and has a broad line width. The dielectric function of water can be described by the two-component Debye model with the Lorentz term [118, 123]:

$$\begin{aligned} \epsilon(\omega) = \epsilon_\infty + \frac{\epsilon_s - \epsilon_1}{1 + i\omega\tau_d} + \frac{\epsilon_1 - \epsilon_\infty}{1 + i\omega\tau_2} + \\ + \frac{A}{\omega_0^2 - \omega^2 + i\omega\gamma} + \dots \end{aligned} \quad (5.30)$$

where

$$\epsilon(\omega) = \left[n'(\omega) - i\alpha(\omega) \frac{c}{\omega} \right]^2, \quad (5.31)$$

$$n'(\omega) = \text{Re} \left[\sqrt{\epsilon(\omega)} \right], \quad \alpha(\omega) = \frac{\omega}{c} \text{Im} \left[\sqrt{\epsilon^*(\omega)} \right]. \quad (5.32)$$

In Eq. (5.30): $\tau_d = 9.36$ ps, $\tau_2 = 0.3$ ps are the slow and fast relaxation times; $\epsilon_\infty = 2.5$ is the susceptibility at high frequencies; $\epsilon_s = 80.2$, $\epsilon_1 = 5.3$ are the contributions to susceptibility from the first and second Debye additives; $A = 38$ (THz/2 π)², $\omega_0 = 5.6$ THz/2 π , $\gamma = 5.9$ THz are the amplitude, frequency, and bandwidth of Lorentz additive, respectively. All constants are taken for 20°C. The reflection, absorption, and refraction spectra of liquid water calculated using Eqs. (5.30)–(5.32) are presented in Fig. 5.6 together with the measured spectra. The absorption and refraction spectra of many soft biological tissues have a similar shape but with less magnitude of absorption. Because the high sensitivity of the ATR method exists only for superficial tissue layers up to approximately 10 μm , the skin is probed only by the depth of the horny layer in which the water content is minimal ($\sim 15\%$). This layer consists mainly of proteins ($\sim 70\%$) and lipids ($\sim 15\%$), and therefore the reflection spectrum of skin differs considerably from that of water.

The strong absorption of liquid water limits the applicability of THz pulses for tissue studies, however THz spectroscopy has been established as a technique to probe biomolecular hydration, binding, conformational change, and oxidation state change. Considerable reduction of THz pulse absorption and index of refraction for soft tissues can be achieved by reversible tissue dehydration at topical application of hyperosmotic agents similar to that used for tissue optical clearing [29, 118, 123, 124] (see section 3.7).

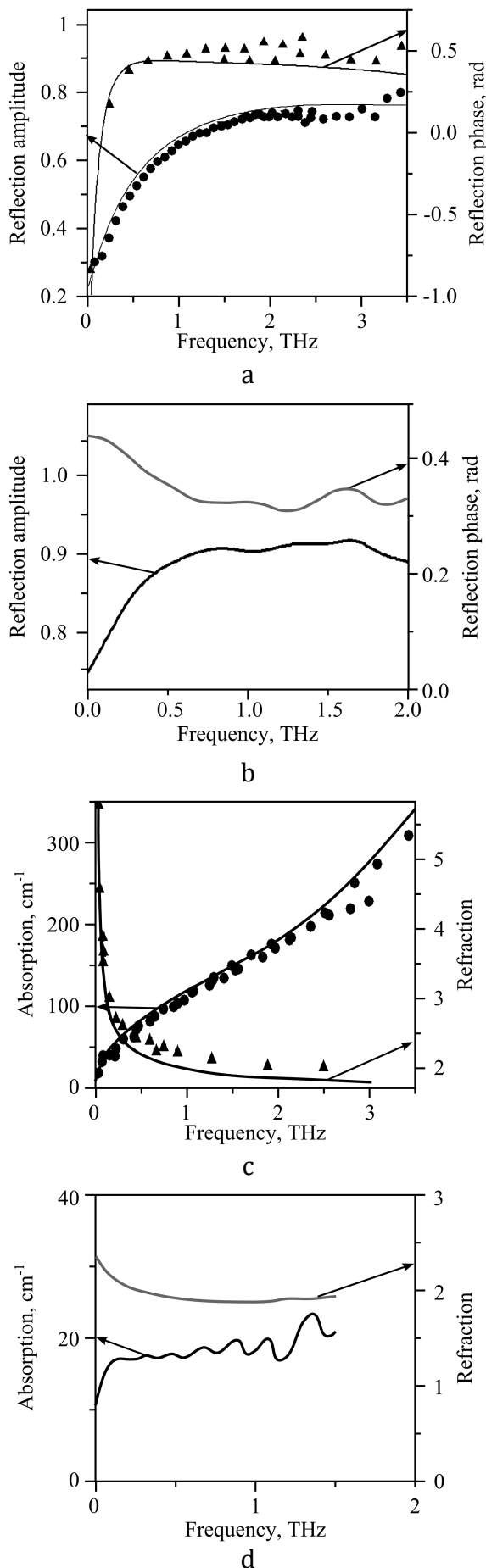


Fig. 5.6 The attenuated total internal reflection (ATR) THz spectroscopy: the reflection (amplitude and phase), absorption, and refraction spectra of liquid water (calculated and experimental) and human skin (measured *in vivo* for Caucasian palm skin of 32 year male volunteer); calculations were done using Eqs. (5.30)–(5.32) for the two-component Debye model with the Lorentz term with $\tau_d=9.36$ ps, $\tau_2=0.3$ ps, $\epsilon_\infty=2.5$, $\epsilon_s=80.2$, $\epsilon_1=5.3$, $A=38(\text{THz}/2\pi)^2$, $\omega_0=5.6$ THz/ 2π , and $\gamma=5.9$ THz at 20°C; (a) and (c) – water; (b) and (d) – skin; (a) and (b) – reflection amplitude and phase; (c) and (d) – absorption and refraction; graphs from M.M. Nazarov [118, 123].

6 Photochemical interactions

6.1 General remarks

Photochemical interactions of light and tissue is of great interest for the study of tissue damage induced by solar radiation, in particular in skin-aging process, as well as for the designing of controllable technologies for tissue repairing and rejuvenation. Such interaction depends on the type of endogenous or exogenous chromophore (photosensitizer) involved in photochemical reaction, oxygen tension, and light wavelength, intensity, and exposure [1-15, 23, 19-26, 34, 51, 125-157]. To characterize a photochemical reaction a quantum yield is introduced. For a radiation-induced process, quantum yield is the number of times that a defined event (usually a chemical reaction step) occurs per photon absorbed by the system. It is a measure of the efficiency with which absorbed light produces some effect. Since not all photons are absorbed productively, the typical quantum yield is less than 1. Quantum yields greater than 1 are possible for photo-induced or radiation-induced chain reactions, in which a single photon may trigger a long chain of transformations.

The major of photochemical reactions is induced by the short wavelength light ($\lambda < 320$ nm) (see Fig. 1.1). For many biological systems, such reactions as photodissociation (breaking down a molecule into radicals and ions) and photoassociation (binding of two molecule monomers) are characteristic [3, 15, 23, 51]. Photodissociation, photolysis, or photodecomposition is a chemical reaction in which a chemical compound is broken down by photons. It is defined as the interaction of one or more photons with one target molecule. Any photon with sufficient energy can affect the chemical bonds of a tissue chemical compound. Photons of visible light or higher energy, such as ultraviolet, X-ray and gamma ray photons, are usually involved in such reactions. There are a number of other photochemical reactions, including photodimerisation — reaction producing a compound formed by combination of two identical molecules. Photoisomerisation is the process by which one molecule is transformed into another molecule which has exactly the same atoms, but the atoms are rearranged. Photohydration is the binding of molecule of water. Photooxidation is the light-induced

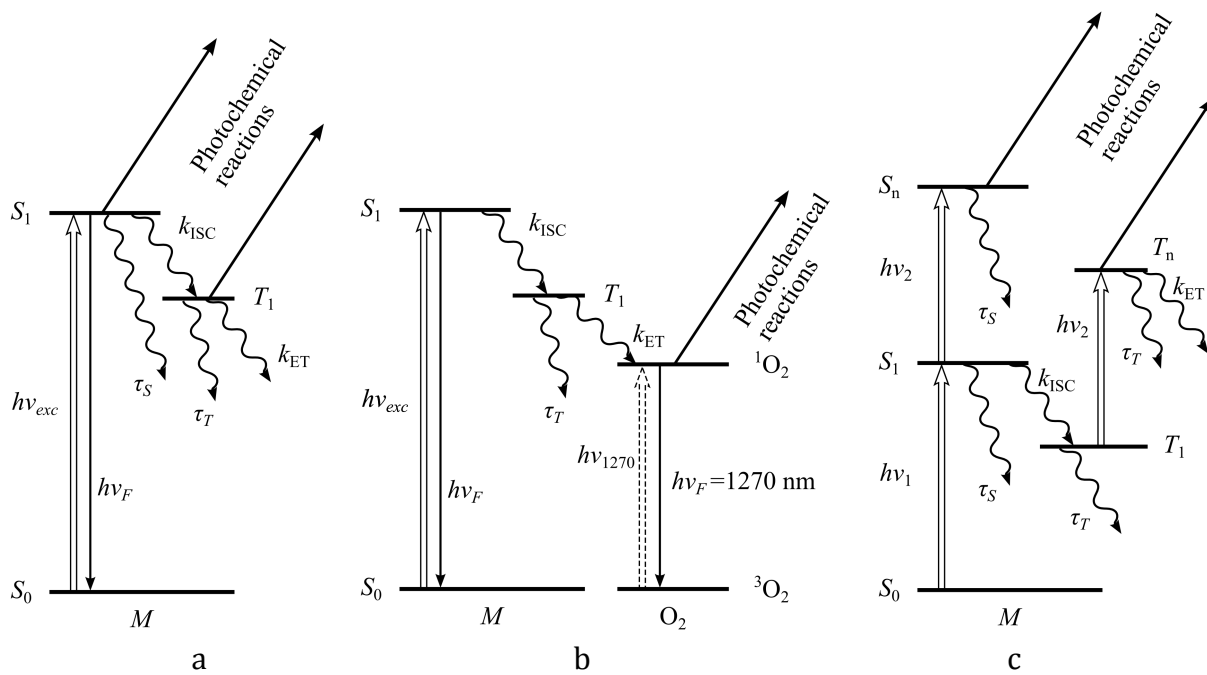


Fig. 6.1 Types of molecular photophysical/photochemical reactions: (a) – one-photon excitation ($h\nu_{exc}$) of molecules (M) followed up by fluorescence ($h\nu_F$) and photochemical reaction; (b) – one-photon excitation of molecules of a photosensitizer (M) followed up by fluorescence ($h\nu_F$) and energy transfer to molecular oxygen (3O_2) with generation of singlet oxygen (1O_2), 1O_2 may then cause biochemical changes with nearby molecules in the cells or tissue or may decay radiatively to 3O_2 , emitting a near-infrared photon $h\nu_F = 1270$ nm; with some efficiency 1O_2 -level can be directly excited by NIR light (1270 nm), $h\nu_{1270}$; (c) – two-photon excitation of the higher singlet and triplet energy levels of molecule M and follow up photomodification or energy transfer to other molecules; $S_0 \rightarrow S_1$, $S_1 \rightarrow S_n$, $T_1 \rightarrow T_n$, and $^3O_2 \rightarrow ^1O_2$ – light absorption; $S_1 \rightarrow T_1$ – intersystem crossing, k_{ISC} (see Fig. 4.4); energy transfer to 3O_2 or other molecules, k_{ET} (see Fig. 4.4); τ_S – total decay time of excited singlet levels, radiative and nonradiative; τ_T – total decay time of excited triplet levels, radiative (phosphorescence) and nonradiative [3, 15].

interaction between oxygen molecules and all the different substances they may contact, from metal to living tissue. More precisely, it is defined as the loss of at least one electron when two or more substances interact, which may or may not include oxygen. Sensitized photooxidation by singlet oxygen molecules, produced at interaction of light-excited molecules of the photosensitizer with oxygen, is an important example of the photochemical processes. The opposite of photooxidation is photoreduction — the addition of at least one electron when substances come into contact with each other at light irradiation. All these reactions lead to structural changes of a tissue, including processes of photodestruction.

Light-controlled biochemical reactions are the basis for laser or light therapy. Laser light is principle to use at multiphoton excitation when a high density of photons is needed which is practically unattainable with the other light sources [3, 15, 23]. Two schemes, presented in Figs. 6.1a,b, are basic for linear one-photon photobiology; excited molecule either directly taking part in a photochemical reaction (Fig. 6.1a), or transfer its energy to other molecule, contributing to biochemical changes (Fig. 6.1b). To make processes effective, the excitation rate W_{exc} , which is proportional to photon density of light, should be higher than

relaxation time of the excited states, $1/\tau_{S,T}$. The third scheme (Fig. 6.1c) is the basis for nonlinear multiphoton photobiology and realized at the laser intensities when a molecule may absorb more than one photon.

One-photon photobiochemical processes are basic for therapy in infants with neonatal jaundice – unconjugated hyperbilirubinemia (the presence of excess bilirubin in the blood) [142]; phototherapy or photochemotherapy of skin, for example such as PUVA (psoralen + UVA) therapy for treatment of psoriasis, eczema, vitiligo and other skin diseases; psoralens are photosensitizing agents found in plants (the parent compounds in a family of natural products known as furocoumarins) [23, 128, 138]; and photodynamic therapy (PDT) of tumors and inflammatory diseases with the usage of hematoporphyrin derivative (HPD), aluminum phthalocyanine tetrasulfonate, methylene blue and other photosensitizers absorbing in the far red of the visible range (Fig. 6.2) [23, 127, 129-132, 137, 139-141].

In application to psoriasis treatment PUVA therapy the diseased skin is typically impregnation by a psoralen as a photosensitizer (absorbing peaks at 295 and 335 nm) and UVA radiation provides the phototoxic effect – reduction of cell abnormal proliferation due to cross-

linking of DNA molecules in the cell nuclei [23, 128, 138].

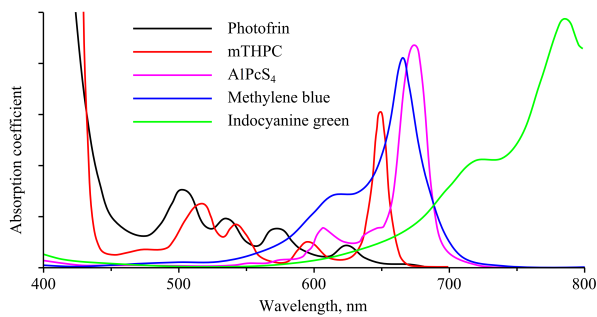


Fig. 6.2 Absorption spectra of some representative PDT photosensitizers: Photofrin® – hematoporphyrin derivative; mTHPC – m-tetrahydroxyphenylchlorin; ALPcS₄ – aluminum phthalocyanine tetrasulfonate; methylene blue, 0.1% in glycerol (650 cm⁻¹ for the peak); indocyanine green, 2 mg/ml in ethanol-glycerol-water solution (1600 cm⁻¹ for the peak) [15, 23, 130].

In PDT injected in the blood stream or topically applied molecules of a photosensitizer have a tendency to be accumulated in the tumor cells due to their high proliferative activity. These molecules are well excited by the visible light (see Figs. 6.1, 6.2) and can transfer excitation energy via their triplet state to oxygen molecules dissolved in tissue (Fig. 6.1b). In its turn, oxygen molecules are excited in the chemically active singlet state (¹O₂) and induce cell damage reactions. The selectivity of HPD accumulation (cell uptake) by tumors in comparison with normal tissue in 2–3 days after systemic injection is of 5:1. The most active component of HPD – Photofrin II has even more selectivity –10:1.

The HPD absorbs light with 620 nm which well penetrates into tissue. There are a plenty of novel photosensitizers absorbing light in the far red and NIR providing effective tumor cell killing or photodamage of blood vessels supplying tumors at reasonable depth in tissues (see Fig. 6.2).

6.2 Photodynamic therapy (PDT)

In clinical medicine the term PDT is generally defined as the use of a compound or drug (photosensitizer) that has no or minimal effect alone but which, when activated by light, generates one or more reactive chemical species that are able to modify or kill cells and tissues. As historically defined, the PDT reaction should be mediated by oxygen, through the generation of reactive oxygen, most commonly singlet oxygen (¹O₂), however, there are photosensitizers that may use oxygen-independent photophysical pathways which could be considered as photodynamic agents also [87, 88, 127, 129-132, 137, 139-141, 143-153].

There are many different PDT photosensitizers and several ‘hardware’ technologies required to apply PDT in patients, including different light sources (lasers, LED matrices and filtered lamps), light delivery devices (based particularly on optical fibres to reach deep within the body), and ‘dosimetry’ instruments to measure the

local light intensity or photosensitizer concentration or oxygen concentration, or combinations of these [130]. At the cellular level, there is good understanding of the basic mechanisms of PDT-induced damage, with one or more different mechanisms of cell death being involved (necrosis, apoptosis, autophagy), depending on the PDT parameters and cellular characteristics. Likewise, tissue may be modified or destroyed by PDT either directly by the cell death or indirectly by disruption of the vasculature, and both local and systemic immune responses can be involved in some cases. The multi-component nature of the photophysical, photochemical and photobiological processes (Fig. 6.3) in PDT make it a challenging modality to optimize, and much of the clinical progress to date has been largely empirically based. Novel PDT technologies include photodynamic molecular beacons in which the photoactivation is quenched until the molecules reach specific targets, the use of nanoparticles, either as photosensitizers or as carriers thereof, and the use of ultrashort pulsed laser activation in two-photon PDT (see Fig. 6.1) [130].

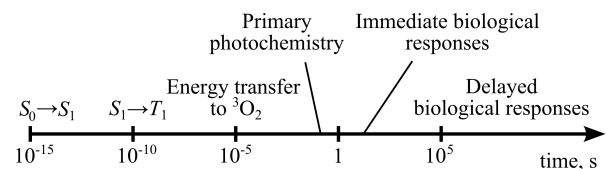


Fig. 6.3 Order-of-magnitude time scales for the sequence of photophysical/photochemical/biological events in PDT: $S_0 \rightarrow S_1$ – light absorption; $S_1 \rightarrow T_1$ – intersystem crossing, k_{ISC} ; energy transfer to ³O₂, k_{ET} ; (see Figs. 4.4 and 6.1) [15, 130].

Many PDT photosensitizers are also fluorescent, thus could be used for photodynamic diagnoses (PDD), i.e. PDT belongs to theranostics. Theranostics is a term composed from two words: therapy and diagnostics. It related to a clinical technology where in the framework of a similar approach both diagnostics and therapy are provided. The unique feature of PDD/PDT technology is that it allows for easy combination of diagnoses (imaging) and treatment using the same instrumentation by only change the laser output power [130].

There are numerous different PDT photosensitizers that have been used in patients to treat a wide variety of diseases, from cancer to infection and abnormal blood vessel proliferation. Hematoporphyrin derivative (HpD) was the first PDT photosensitizer in investigation of the mechanism and clinical application for cancer detection and treatment in early 1970s. The HpD useful excitation band is around 620–630 nm (see Fig. 6.2), it is efficient with typical light dose of 150 J/cm². Photofrin II (Photofrin®) – a purified form of HpD was approved for treatment of bladder cancer in Canada in 1993. Photofrin®, Photosan®, and Photogem® are the commercialized products. The second-generation HpD photosensitizers, such as HMME (hematoporphyrin monomethyl ether), PsD-007 (photocarcinorin), and HiPorfin are also available [23].

The discovery of endogenous photosensitization of protoporphyrin IX (Pp IX) induced by exogenous administration of prodrug ALA (delta-aminolevulinic acid) allowed for treatment of pre-malignant and malignant skin lesions at topical ALA application [23, 130]. Clinical studies with ALA-PDD/PDT drugs Levulan®, Alasens®, and Metvix® (MLA – a methyl ester of ALA) showed their efficiency for the treatment of actinic keratoses, squamous cell carcinomas and basal cell carcinomas.

Temoporfin (mTHPC – m-tetrahydroxyphenylchlorin), mono-L-aspartyl chlorine e6 (NPe6, LS11, talaporfin sodium, or MACE), and purpurin are photosensitizers of chlorin family with an excitation band around 652–664 nm (see Fig. 6.2). The commercialized products are Foscan® (mTHPC, approved in Europe in 2001, PDT light dose is 20 J/cm²), Laserphyrin® (mono-L-aspartyl chlorine e6, approved in Japan in 2004 for PDT of lung cancer, PDT light dose is 100 J/cm²), and Purlytin® (purpurin, PDT light dose is 200 J/cm²) [23, 130].

Photosens® is a PDT photosensitizer, which contains a mixture of sulfonated aluminium phthalocyanines with various degrees of sulfonation. Spectrum of AlPcS₄ (aluminum phthalocyanine tetrasulfonate) is shown in Fig. 6.2. Photosens® requires laser light of a specific wavelength of 675 nm for activation; it has been designed in Russia and tested for various disease, including treatment of age-related macular degeneration, PDT typical light dose of 100 J/cm² [23, 130].

Benzoporphyrin derivative (BPD) is a photosensitizer with an excitation band around 690 nm. Verteporfin® and Visudyne® for injection (benzoporphyrin derivative monoacid ring A (BPD-MA)) are the commercialized products; at PDT typical light dose is of 100 J/cm² [23, 130].

Texaphyrins are photosensitizers of porphyrin family with an excitation band around 730 nm. Lutetex®, Lutrin®, Optrin®, and Antrin® are the commercialized products. PDT typical light dose is 150 J/cm². Antrin® contains motexafin lutetium (pentadentate aromatic metallotexaphyrin). For activation it requires laser light of a specific wavelength 742 nm with fluence 75 J/cm² at a power density 75 mW/cm². It is used to treat skin conditions and superficial cancers, it has also been tested for use in photoangioplasty (PDT treatment of diseased arteries) [23, 130].

TOOKAD® (WST09) contains palladium bacteriopheophorbide. For activation it requires light of a specific wavelength 763 nm with fluence in the range 50–200 J/cm² at 150 mW/cm². It can be used to treat relatively large solid tumours, such as localized prostate cancer. In *in vivo* applications the most prominent feature of TOOKAD is its fast clearance, while exclusively staying within the vascular network. Because of these properties, TOOKAD-mediated PDT causing extensive vascular damage, thus, is also referred to as vascular-targeted PDT (VT-PDT) [23, 130].

Indocyanine green (ICG) is a water-soluble tricarbocyanine dye with infrared absorbing and fluorescing properties. ICG was approved by FDA as an absorbing and fluorescent agent for biomedical diagnostics. In water its absorption is peaked at 775 nm with little or no absorption in the visible below 700 nm (see Fig. 6.2). In tissues and cells, the NIR absorption peak due to binding with cell proteins is moved to longer wavelengths to 805 nm for blood and human skin *in vivo*, and to 810 nm for epidermal cell cultures [23, 143, 146–149]. It has a photodynamic effect and used for bacteria killing in tissue depth such as *Propionibacterium acnes* at skin acne treatment using PDT with a NIR diode laser (810 nm).

Methylene blue (MB) is also one of the biological dyes (photosensitizers) showing a phototoxic effect and is prospective to use in inflammatory disease treatments [23, 150]. Its absorption bands in the visible range are at 609 and 668 nm (Fig. 6.2). It can be activated by light to an excited state, which in turn activates oxygen to yield oxidizing radicals.

In PDT reaction of type I, the chemical changes in the biomolecules are caused by direct interactions of either the excited singlet (S_1) or much more probably triplet (T_1) states themselves of the photosensitizer, without the energy transfer to oxygen with singlet oxygen generation (see Fig. 6.1a). The singlet state (S_1) is formed by absorption of a photon of light by a ground-state photosensitizer molecule (S_0): $S_0 \rightarrow S_1$, as triplet state is generated by the intersystem crossing process $S_1 \rightarrow T_1$ with a rate constant k_{ISC} .

However, the type II reaction, where biochemical interactions are produced indirectly by the singlet oxygen 1O_2 which is generated by excitation of the ground-state oxygen (3O_2) that is dissolved in the cells or tissues by energy exchange process with a rate constant k_{ET} from the triplet state (T_1) of the photosensitizer (Fig. 6.1b), is characteristic for the most PDT photosensitizers [23, 151].

Important to note, that 1) the photosensitizer state S_0 is cyclically regenerated and the absorption process $S_0 \rightarrow S_1$ may occur many thousand times for a given molecule during a PDT treatment; 2) the ground state of oxygen (3O_2) is unusual regarding other molecules in being a triplet state, making the $T_1 \rightarrow ^3O_2$ transition quantum-mechanically allowed (no change of spin), that provides for photosensitizers high quantum yields to generate 1O_2 ; 3) the energy gap between the excited and ground-state oxygen molecules ($^3O_2 \rightarrow ^1O_2$) is close to 1 eV, so that this would be the minimum photon energy required to trigger the reaction; however in practice, the efficiency of 1O_2 production is limited to photon energies about 1.5 eV, corresponding to wavelengths around 800 nm, which corresponds to the longest wavelength of PDT activation of 763 nm using a bacteriopheophorbide photosensitizer (TOOKAD®) and ICG (775–810 nm) [130].

The various excited states in Fig. 6.1 may de-excite either radiatively, i.e., with the emission of visible or near-infrared (NIR) light ($h\nu_r$), or nonradiatively

(internally by energy transfer as in $T_1 \rightarrow {}^3\text{O}_2$ (k_{ET}), or by collisional de-excitation with other molecules resulting in heat with the total decay time of excited singlet and triplet levels (radiative and nonradiative), τ_S and τ_T). The $S_1 \rightarrow S_0$ transition with fluorescence emission ($h\nu_F$) is the basis of PDD [130, 152]. The higher quantum efficiency of singlet oxygen (${}^1\text{O}_2$) generation, the lower is the fluorescence quantum yield. However, the typical fluorescence quantum efficiency is of a few percent which is acceptable to provide fluorescence spectroscopy/imaging (marking of the lesion borders on the cellular level). Fluorescence is also used for evaluation of the photosensitizer uptake prior to light activation for PDT and also, through photobleaching, for PDT light dosimetry. The fluorescence lifetime of PDT photosensitizers is typically in the ns range.

Since $T_1 \rightarrow S_0$ transition is quantum-mechanically forbidden, the corresponding phosphorescence emission has low probability for most PDT photosensitizers, thus the T_1 state is long lived ($\sim \mu\text{s}$), which increases the probability of energy transfer to ground-state oxygen and, hence, generation of ${}^1\text{O}_2$. The energy of molecular oxygen radiative transition ${}^1\text{O}_2 \rightarrow {}^3\text{O}_2$, i.e., decay of singlet oxygen back to the ground state, corresponds to a wavelength of around 1270 nm. The detection of this rather weak radiation is the basis for so-called SOLD (singlet oxygen luminescence dosimetry) in PDT [130]. The ${}^1\text{O}_2$ lifetime in water is about 3 μs . The lifetime is believed to be an order-of-magnitude shorter in cells and tissues due to the high reactivity of ${}^1\text{O}_2$ with biomolecules. Assuming that the lifetime is short, the diffusion distance, i.e., the average distance travelled by a molecule of ${}^1\text{O}_2$ before it interacts, could be very short, as low as 10 nm. Hence, the chemical damage and consequent biological effects of ${}^1\text{O}_2$ should be extremely dependent on the localization of the photosensitizer molecule at the time of excitation [139-141].

The generated ${}^1\text{O}_2$ molecule is responsible for chemical alterations in target biomolecules in the cell or tissue, resulting in various biological effects. The order-of-magnitude time scales for the sequence of photophysical-photochemical-biological events in PDT from 10^{-15} to 10^5 s schematically presented in Fig. 6.3 [129, 130].

The light intensities needed in PDT are not high, less than or equal to 1 W/cm^2 , for many cases the power density 150 mW/cm^2 at energy dose of $20 - 200 \text{ J/cm}^2$ is sufficient, and could be provided by lamps and other light sources [15, 29-24, 154]. However often laser radiation is preferable, because of easy delivery with fibers to any site of body including internal organs; extremely high laser light brightness allows one to reduce irradiation time, therefore lasers were a driving force in PDT development; and, finally, sometimes with the help of a pulse laser the needed dose is possible to provide by a single shot that allows one to exclude effects of light on the follow up biochemical reactions.

To enhance efficiency of photo-treatment combined light interaction phenomena are used [144-146, 153].

For dual-modality photodynamic and photothermal treatment of tumors *in vivo*, gold nanorods with hematoporphyrin-loaded silica shell were effectively employed [144]. Enhanced photoinactivation of *Staphylococcus aureus* induced by red or NIR laser radiation was provided using conjugates of plasmon-resonance nanoparticles with hematoporphyrin [145] or indocyanine green [146]. Multifunctional gold nanoclusters for targeted bioimaging and enhanced photodynamic inactivation of *Staphylococcus aureus* were also recently suggested [153].

6.3 Low level light therapy (LLLT)

For some diseases to provide phototherapy no any exogenous photosensitizers are needed and intensity of light could be low, but with a particular wavelength, light dose and light pulse parameters. This is a so called low level light therapy (LLLT) which uses low intensity visible or near infrared light for reducing pain, inflammation and edema; promoting healing of wounds, deeper tissues and nerves, and preventing tissue death [121, 125, 126, 133-135, 137]. LLLT is still a controversial treatment technology which is connected with the lack in understanding of the biochemical mechanisms underlying the positive effects and corresponding difficulties in finding of a proper irradiation parameters, such as wavelength, fluence, power density, pulse structure, and treatment duration. However, due to used low intensities which are in the limits of laser safety standards [155, 156] no any tissue damage is expected and the probability of adverse effects is very low.

The first law of photobiology states that without any absorption there can be no biological responses (see Fig. 6.3). The visible and NIR photons are absorbed by tissue intrinsic molecules—chromophores at their light induced electronic transitions $S_0 \rightarrow S_1$ (see Figs. 4.4 and 6.1) within electronic absorption bands. With the depth of penetration and absorption obtained with photons at selected wavelengths there is absorption in all tissue cells at all levels, including blood vessel endothelial cells and erythrocytes. To find the identity of chromophores one is able to carry out an action spectrum which is the rate of a physiological activity measured and plotted against the wavelength of activating light (see sections 3.1 and 3.2). It shows which wavelength of light is most effectively used in a specific photochemical or photobiology reaction.

It was suggested in 1989 by T. Karu that the mechanism of LLLT at the cellular level is based on the absorption of monochromatic visible/NIR radiation by components of the cellular respiratory chain associated with mitochondria which play an important role in energy generation and metabolism [125,126]. The mitochondrial respiratory chain (electron transport chain) consists of a series of metalloproteins (cytochrome enzymes) bound to the inner membrane of the mitochondria. However, the high specific absorption spectrum of one of them, such as cytochrome *c* oxidase (or cytochrome complex IV, or cytochrome-*aa*₃) with a

distinctive absorption bands in the red (~600 nm) and NIR (820–830 nm) (see Fig. 3.6), coupled with its high concentration, means that cytochrome *c* oxidase (Cox) is the enzyme of most interest in LLLT. Absorption spectra obtained for Cox in different oxidation states were found to be very similar to the action spectra for biological responses to light and allowed to consider Cox as the primary photoacceptor for the red/NIR light in mammalian cells. In addition, increased activity of Cox and an elevation in measured oxygen uptake were observed in illuminated mitochondria.

Such endogenous chromophores as porphyrins (see Fig. 3.6) are formed in mitochondria as part of the heme biosynthesis cycle. The absorption spectrum of one of most important from this family of porphyrins like protoporphyrin IX (Pp IX) in the region from 400 nm to 630 nm has five bands decreasing in size as they move toward the red: 403 (Soret band), 504, 535, 575, and 633 nm (Q bands). The presence of Pp IX in cells and tissues as a result of the metabolic activity allow one to consider the “singlet-oxygen hypothesis” basic for PDT to be one of the important pathways for LLLT. As a direct proof of the possibility of this mechanism to be involved in biostimulation the numerous experimental facts that very low doses of PDT can cause cell proliferation instead of the killing observed at high doses [157].

Molecules of flavoproteins (proteins that contain a derivative of riboflavin), such as flavin adenine dinucleotide (FAD) or flavin mononucleotide (FMN) (see Fig. 3.6) also might act as photoacceptors and mediate a particular biochemical reaction in cells and tissues due to their involvement in a wide range of biological processes, including bioluminescence, removal of radicals contributing to oxidative stress, photosynthesis, DNA repair, and apoptosis [15, 125, 126, 133-135].

As we already discussed both the absorption and scattering of light in tissues depend on the wavelength being much higher in the blue than in the red/NIR range and define therefore the penetration depth of light, which is maximal in NIR. The principle tissue chromophores, such as melanin and hemoglobin (see Figs. 3.5 and 3.6), have strong and broad absorption bands at wavelengths shorter than 600 nm: at ~335 nm for melanin and ~415 nm and 542–577 nm for hemoglobin. Therefore, the UVA/blue/green/yellow light may have significant effects on cells growing in optically transparent culture medium. Nevertheless, the use of LLLT in patients almost exclusively involves red/NIR light (600–950 nm) due to its high penetration depth in spite of less efficiency of light-induced photochemical processes.

The evidence suggesting that mitochondria are responsible for the cellular response to red/NIR light was proved by experiments on isolated mitochondria with irradiation by light at one of the following wavelengths 633, 650, 660, or 725 nm and approximate dose of 5 J/cm² [15, 125, 126, 133-135]. A plenty of biochemical responses was found, including increase in

proton electrochemical potential, oxygen consumption, membrane potential and proton gradient, the rate of ADP (adenosine diphosphate)/ATP (adenosine-5'-triphosphate) exchange, as well as enhanced synthesis of NADH, ATP, RNA and proteins. It is also believed that mitochondria are the primary targets when the whole cells are irradiated with light at 630, 633, or 820 nm.

Several classes of molecules, such as reactive oxygen species (ROS) and many others, are involved in the signaling pathways from mitochondria to nuclei for controlling the expression of individual genes via a corresponding transcription factor. This is a so called redox signaling – a regulatory process in which the signal is delivered through redox (redox state) chemistry to induce protective responses against oxidative damage. It was found experimentally in cell *in vitro* studies that LLLT increases ROS generation and cell redox activity. Depending on the signal networks that a cell operates after illumination, it may change the rate of proliferation, or die via apoptosis [15, 133, 134].

The ability of light to influence the localized production or release of nitric oxide (NO) and stimulate vasodilation through the effect NO on cyclic guanosine monophosphate (cGMP) was demonstrated in many studies [15, 125, 126, 133, 134, 158]. The cGMP is a common regulator of ion channel conductance; it relaxes smooth muscle tissues leading to vasodilation of blood vessels and increased blood flow. The cGMP is also a regulator of cellular apoptosis. It is known that NO inhibits the activity of Cox. It has been proposed that VIS/NIR light can reverse the inhibition caused by NO binding to Cox by photodissociating NO from the Cox, thus to protect cells against NO-induced cell death. In experiments with the visible and NIR light (600...630 nm, 780 nm, and 804 nm) a significant increases of NO in illuminated tissues after LLLT was detected. In contrast for some studies in tissues irradiated by red and NIR light reduction of NO have been found. It was explained by proposing that light may inhibit inducible NO-synthase.

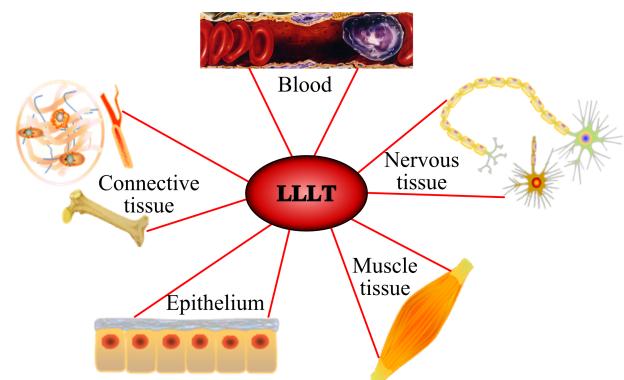


Fig. 6.4 Low-level light therapy (LLLT), tissue and blood effects [133, 134].

It follows from above that mechanisms of LLLT are still not clearly understood. Nevertheless, *in vitro* studies evidently prove that VIS/NIR light of the

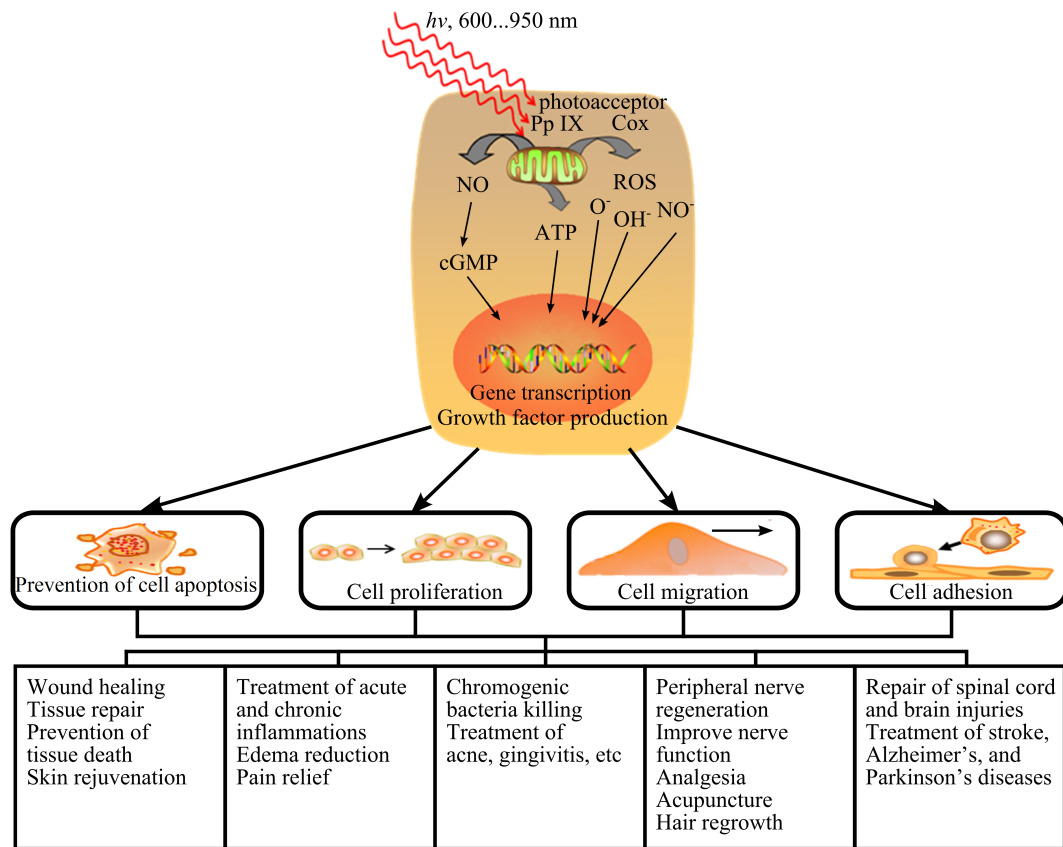


Fig. 6.5 A simplified schematic representation of the main cellular and tissue effects of LLLT and areas of its application; Pp IX – protoporphyrin IX; Cox – cytochrome *c* oxidase; NO – nitric oxide; cGMP – cyclic guanosine monophosphate; ATP – adenosine-5'-triphosphate; ROS – reactive oxygen species [133, 134].

appropriate wavelength, intensity and dosage can prevent cell apoptosis and improve cell proliferation, migration and adhesion, and support the clinical application of LLLT [133, 134].

Proliferation of fibroblasts, keratinocytes, endothelial cells, and lymphocytes can be enhanced at light fluence of 2 J/cm², but cell status and nutritional conditions are critical to provide cell growth [133, 134]. This is a basis for a number of LLLT technologies. Figure 6.4 shows schematically the applicability of LLLT for different tissue types, such as epithelial, connective, muscular, and nervous tissues. For epithelial tissues, light-activated cell proliferation, migration, and adhesion are key processes (Fig. 6.5). Activated cell secretion of different growth factors (vascular endothelial growth factor and transforming growth factor-β) is also important. The LLLT can increase collagen synthesis by fibroblasts, provide an effective lymphatic drainage, enhance neovascularisation, promote angiogenesis, and increase blood flow.

Laser treatment at 655 and 810, 830 nm with the dosage of 0.5–1.0 J/cm² has been shown to promote proliferation of different types of muscle cells including skeletal muscle, smooth muscle, and cardiac muscle. The beneficial effect of phototherapy on the process of muscle repair processes after injury or ischemia in

skeletal and heart muscles as well as preventing development of muscular fatigue were shown.

The usage of LLLT for wound healing is based on light-induced stimulation of fibroblast migration, proliferation, and metabolism to accelerate wound closure. For example, Karu's experiment indicated that pulsed NIR radiation at 820 nm increases the cell-matrix attachment [125, 126]. Several biological mechanisms connected with cytokine and growth factor expression are involved in wound healing process [133]. These are cytokines responsible for the initial inflammatory phase of wound healing, as well as fibroblast proliferation, migration, and transformation into myofibroblasts; and growth factors responsible for the neovascularization and inducing collagen synthesis from fibroblasts. Hamblin and co-workers found for 635-nm light a maximum positive effect in wound healing at light dose of 2 J/cm² [133, 134]. Amongst 635-, 670-, 720-, and 820-nm wavelengths tested, 820-nm was the best. No difference between coherent and incoherent light treatment was revealed. Biochemical response on laser light is significantly depends on the pulse repetition rate, for fibroblasts irradiated by diode laser with λ = 904 nm and pulse width of 150 ns, at dosage of 7 mJ/cm², the optimal pulse repetition rate was found as 67 Hz.

LLLT (633, 830 nm) was reported to affect the proliferation and maturation of human osteoblasts cells, bone repair in mice, and increase histological parameters of immobilized articular cartilage in rabbits [133].

LLLT may be effective in treatment of chronic inflammatory conditions by preventing release of cytochrome c into the cytoplasm, and therefore prevention of cell apoptosis. It was shown that NIR phototherapy could reduce the rate of apoptosis by 50%. LLLT was conducted into different animal model of inflammatory disorders such as burns and peritonitis [133].

LLLT found to be an effective treatment in patients with the painful inflammation diseases, such carpal tunnel syndrome, arthritis, osteoarthritis, tendonitis, shoulder injuries, muscle spasm, myofascitis, fibromyalgia, and mucositis. LLLT using CW lasers with power in the range 10–250 mW, selected wavelengths of 633, 660, 670, 780, 810, 830, or 930 nm and dosage of 0.7–35 J/cm², as well as pulsed 904-nm infrared laser with the output pulse power of 9.4 W, have a significant effect in these patients [133, 134]. A rather big variety of used dosages is due to different light penetration depth defined by the wavelength and thickness of a particular tissue. In clinical studies with many patients with joint disorders, LLLT reduced pain by 70% relative to placebo and reduced morning stiffness. In the treatment of painful conditions related to chronic neck and lower back pain, tendonitis, chronic joint disorders, temporomandibular joint pain-dysfunction syndrome, trigeminal neuralgia, postherpetic neuralgia, and diabetic neuropathy, LLLT is also an effective tool.

In support of inhibitory mechanisms are a number of studies that demonstrate that CW 830-nm radiation slows nerve conduction velocity and increases latencies in median and sural nerves. Another mechanism for a neural basis of laser-induced pain relief is based on the blocking of the axonal flow of small-diameter nerves, which resulted in a decrease in mitochondrial membrane potential with a concurrent decrease in available ATP required for nerve function [133, 134].

The very important application of LLLT to the central nervous system, that includes repair of spinal cord injuries, reduction of brain damage after stroke and traumatic brain injury, and the treatment of degenerative brain conditions such as Alzheimer's and Parkinson's diseases [134]. Therefore light-induced nerve regeneration and repair is becoming a rapidly growing field. Animal models have been employed to study LLLT effects in nerve repair. In clinical studies the effectiveness of ischemic stroke treatment in humans was shown when initiated within 24 hours of stroke onset at the application of a hand-held 808-nm laser probe to twenty predetermined locations on the shaved scalp for 2 min in each location with the predicted power density of ~10–15 mW/cm² on the *dura mater*.

The light-induced regeneration of the crushed rat facial nerves was found to be the best for 633-nm laser

with the dosage of 162.4 J/cm² comparing with the other wavelengths tested, such as 361, 457, 514, 720, and 1064 nm. Phototherapy can progressively improve nerve function, and can be used in patients with long-term peripheral nerve injury at 780-nm laser treatment.

Lasers and lamp/LED light sources are finding increased usage in the treatment of such widely spread inflammatory disease as gingivitis or *acne vulgaris* [157, 159]. The blue light is effective due to porphyrins accumulated by *Propionibacterium acnes* and periodontal pathogens *Prevotella nigrescens*, *Prevotella intermedia*, *P. melaninogenica*, *Porphyromonas gingivalis*, the so called chromogenic bacteria which accompany the development of these diseases. Porphyrins absorb blue light and bacteria are killed via PDT action. Green light (540–560 nm) and red light 600–635 nm are also capable to activate porphyrins, but with much less efficiency than blue light. Mixed blue-red light, probably due to combined antibacterial (blue light) and anti-inflammatory action (red light), was shown as an effective tool for treatment of mild to moderate severity *acne vulgaris*.

The clinical efficacy of phototherapy for facile skin rejuvenation with significant reductions of wrinkles and increases of skin elasticity is shown. The light-activated fibroblasts cause the increase in the amount of collagen and elastic fibers. The immunohistochemistry analysis showed the improvement in skin collagen status. Different optical modalities are on use for skin rejuvenation with the dosage of 3 J/cm² of 585-nm laser, with combined wavelengths of 595 nm and 1450 nm, or LED phototherapy with 633 nm or 830 nm.

Basing on the observation that 633-nm laser irradiation with the dosage of 3 J/cm² increases release of the nerve growth factor (NGF) to the medium of myotubes cultured *in vitro*, it is postulated that LLLT may influence hair regrowth via the NGF signaling system [133]. This correlates with a transient elevation of intracellular calcium in the myotubes and finding on significant increase in NGF release from cultured human keratinocytes. A broadband (600–1600 nm) linear polarized 1.8-W light source in treatments of treat alopecia areata produced significant hair growth compared to untreated lesions in 47% of patients. Different light sources, such as lasers with 633 and 670 nm and LED with 635 nm, accompanied by the measurement of blood flow in the scalp were used for male-pattern baldness treatment.

Figure 6.5 presents a simplified schematic of the main cellular and tissue effects of LLLT and the main areas of its application divided into five major groups [15, 26, 133, 134]: 1) wound healing, tissue repairing and protection, skin rejuvenation; 2) treatment of acute and chronic inflammatory diseases, edema reduction, and associated pain relieving; 3) chromogenic bacteria killing for noninvasive treatment of acne, gingivitis, and other microbial associated diseases; 4) peripheral nerve regeneration, improvement of nerve function, analgesia, acupuncture, hair regrowth; and 5) central nervous system diseases treatments including repairing of spinal

cord and brain injuries, treatment of stroke, Alzheimer's, and Parkinson's diseases.

The wavelengths of lasers and LEDs most often used in phototherapy (He–Ne with $\lambda = 633$ nm and He–Cd with $\lambda = 442$ nm; diode GaAs with $\lambda = 830$ nm, or GaPAs and GaInAsP lasers, emitting in the range 640...830 nm and 920...1500 nm, respectively, in dependence on In and P concentration in semiconductor active medium; GaAlAs LEDs with red $\lambda = 650$...700 nm and NIR $\lambda = 710$...850 nm light, GaAs LEDs with NIR $\lambda = 880$...980 nm light and InGaAsP LEDs with NIR $\lambda = 1000$...1550 nm light) are well fit to some wavelength maxima of the action spectra for cell responses: 404, 620, 680, 760 and 830 nm [23]. Besides, in LLLT, UV lasers, i.e. nitrogen, N_2 laser, with $\lambda = 337$ nm, and IR lasers, i.e. CO_2 lasers with $\lambda = 10.6$ μm , are used. Wound or ulcer surface, selected organ or gland, as well as blood in vessels are illuminated intravenously or transcutaneously.

In addition to discussed above endogenous chromophores responsible for biochemical/biological effects, as a potential endogenous light acceptor in the wavelength range 400 — 1300 nm oxygen molecules themselves could be considered (see Fig. 6.1, direct excitation — punctured arrow) [139-141]. Maxima of some absorption bands of molecular oxygen are in the vicinity of the following wavelengths 638, 762, 1060 and 1260 nm. These triplet-singlet transitions are double forbidden. In spite of that in a condensed medium, which is any of tissues, the probability of photoexcitation of the forbidden transitions could be rather high due to weakening of quantum exclusion.

The LLLT often uses lasers, therefore the specificity of coherent light interactions with cells should be considered. As we discussed above a coherent light interaction with optically inhomogeneous tissues induce 3D speckle patterns with a high contrast and speckle size in a micrometer range (see Figs. 3.18 and 3.19). Thus, it could be proposed that the variation in intensity between speckles that are about micron apart can give rise to small but steep temperature gradients within subcellular organelles such as mitochondria. The temperature spatial modulation can cause some unspecified changes in mitochondrial metabolism. Moreover at specific tissue irradiation, for example, using a sharply focused laser beam, speckle contrast can be much more than unity with the intensity of an individual speckle up to ten-twenty times higher than mean intensity of illuminating beam. This can provide temperature or photochemical speckle-induced local stress of cells.

7 Conclusion

This tutorial aimed to provide an overview of the fundamentals and advances of tissue optics and photonics basing on description of light tissue interaction. With this review author attempted to cover a broad range of urgent problems of tissue optics and corresponding imaging and spectroscopy methods used

in biophotonics. Author hopes that this tutorial will help readers to be involved in the research and development in the field of tissue optics and biophotonics. However, with the evidence this tutorial is only a first step to be acquainted with a very broad research field and numerous applications in biology and medicine. Therefore, recommendations for further reading should be done.

Coherent-domain optical methods for biomedical diagnostics, including quantitative phase imaging of cells and tissue slices [160], as well as already broadly commercialized optical coherent tomography (OCT) techniques [161,162], are available for readers as a few volumes of comprehensive monographs written by the pioneers and leaders in the field. Polarized light interactions with tissues are described in recent tutorial published by J. Biomedical Optics [97]. Second harmonic generation imaging techniques are well analyzed in this monograph [27].

Advances of fluorescence microscopy methods and biomedical protocols can be found in the recent monograph [136], where the physical basis and biomedical applications of total internal reflection fluorescence (TIRF) microscopy, light sheet-based fluorescence microscopy, fluorescence resonance energy transfer microscopy (FRET), fluorescence lifetime imaging microscopy (FLIM), fluorescence correlation spectroscopy, structured illumination microscopy, 4Pi, STED and STORM microscopies are presented.

To go in more details in understanding and to do some practical work on optical-thermal response of tissues and cells a few classical monographs can be useful [10, 11, 17, 18].

Basics and advances in photodynamic therapy, including analysis of translational and clinical problems can be learned from recent monographs [129, 131, 132].

The following monographs and text-books cover much broader areas of biomedical optics and tissue photonics, reader will found there consideration of many urgent problems related to tissue and cell optics [15, 19-22, 26, 29, 32-34, 57]. The Dictionary of Biomedical Optics and Biophotonics [23] is useful whether reader is new to the field or needs a robust definition or a brief article on the special topic. It contains approximately 2500 key terms (articles) which give reader a rich understanding of the terminology in this quickly developing field.

Acknowledgments

I am thankful to Valery Zakharov for his idea to write such a paper, to all my colleagues from SSU and IPMC RAS for fruitful collaboration, and to Alexander Kalyanov for help in preparation of illustrations. This work was supported by Russian Presidential grant NSh-7898.2016.2, the Government of the Russian Federation grant 14.Z50.31.0004, and the Ministry of Education and Science of the Russian Federation.